Applied Thermal Engineering 208 (2022) 118201

Contents lists available at ScienceDirect

Applied Thermal Engineering

journal homepage: www.elsevier.com/locate/apthermeng

Research Paper

Thermal-hydraulic performance analysis of a hybrid micro pin–fin, jet impingement heat sink with non-uniform heat flow

H.C. Cui, J.H. Xie, R.Z. Zhao, M.Z. Wang, Z.C. Liu, W. Liu *

School of Energy and Power Engineering, Huazhong University of Science and Technology, Wuhan 430074, China

ARTICLE INFO

Keywords:
Hybrid heat sink
Hotspot-targeted
Energy efficient
Jet impingement
Micro pin–fin array
Non-uniform heat flow

ABSTRACT

Jet impingement as a highly efficient cooling method has been broadly used in the field of heat dissipation for high heat flow electronics. Well-designed structures including jet hole and pin–fin arrangement can significantly alter flow fields to provide a favorable trade between increased heat transfer performance and total pressure loss. In order to solve the imbalance problem of temperature uniformity and power consumption caused by non-uniform heat flux distribution in multi-core integrated circuits, a novel jet impingement cooling concept, for hotspot-targeted, energy efficient cooling of non-uniform heat generation electronics, was proposed in this paper. A three-dimensional numerical simulation was carried out to investigate the effects of jet hole diameter and distribution, heat transfer plate type and inlet area on heat transfer and resistance performance. The heat transfer coefficient, total pressure drop, maximum temperature rise and temperature non-uniformity were selected as the performance parameters. Compared with the traditional jet impingement heat sink, the well-designed heat sink in this work achieves an improvement of 58% in temperature non-uniformity while the total pressure drop is reduced by 68.7% at the same mass flow rate. In addition, the pumping power consumption is only 0.093% and 0.061% of the total heating power for 150 W/cm^2 and 300 W/cm^2 hotspot heat flux respectively while ensuring the acceptable temperature non-uniformity.

1. Introduction

With the continuous development of artificial intelligence in recent years, the demand for chip computing power is higher and higher for the processing of massive data. Hence, multi-core chips or Multi-Processor System-on-Chips (MP-SoCs) come into play to take advantage of parallel execution [1,2]. However, the enhancement of chip computing power and functionality leads to greater chip heat generation with significant non-uniformities, which has exacerbated the integrated device cooling problem and become the main obstacle to the development of integrated circuits in the future [3–5]. In the face of this situation, many traditional cooling methods, such as air cooling and heat pipe cooling, can no longer remove the enormous waste heat in time and maintain the temperature uniformity [6]. Consequently, it is significant to quest an efficient and stable cooling method to ensure the safety and lifetime of electronic devices [7–10]. Compared with traditional cooling methods, microchannel cooling and jet impingement cooling technology, as emerging active liquid cooling technologies, have attracted extensive research interest due to their high cooling efficiency and cooling capacity.

The microchannel cooling technology was first proposed by Tuckerman and Pease in 1981 [11]. By etching microchannels on a silicon substrate for liquid cooling, they found that the heat transfer resistance can be dramatically reduced and then enhance the heat transfer capacity. In the following decades, a lot of experiments and simulations have been carried out to study the channel shape [12–14], internal hierarchical structure [15] and flow pattern [16] of the heat sink so as to improve the heat transfer performance. Although the microchannel heat sink has a compact structure and high heat flux cooling capacity, the large resistance and temperature gradient along the flow direction have become the main obstacles limiting its application [11,17].

As for jet impingement cooling technology, it has been one of the most promising liquid cooling methods due to its extraordinary heat transfer performance, i.e. high heat transfer coefficient in stagnation point, adaptability to local hot spot [18], better synergy of temperature field and velocity field [19]. However, compared with other cooling methods, e.g. microchannel cooling or heat pipe cooling, jet impingement has more complex flow structures, i.e. free jet region, stagnation region and wall jet region, and the essence of flow and heat transfer mechanism is not very clear [20,21]. As a result, further investigations of jet impingement are important in theoretical and practical.

* Corresponding author.
E-mail address: w_liu@hust.edu.cn (W. Liu).

https://doi.org/10.1016/j.applthermaleng.2022.118201
Received 5 July 2021; Received in revised form 19 January 2022; Accepted 5 February 2022
Available online 17 February 2022
1359-4311/© 2022 Elsevier Ltd. All rights reserved.

Nomenclature

A	the area of the heat transfer surface (m^2)
$C_{1\varepsilon}, C_{2\varepsilon}$	constants for RNG $k-\varepsilon$ model
c_p	specific heat at constant pressure ($J\cdot kg^{-1}\cdot K^{-1}$)
D, d	diameter (m)
$h, \overline{h}$	heat transfer coefficient and the average heat transfer coefficient, respectively ($W\cdot cm^{-2}\cdot K^{-1}$)
H	height (m)
k	thermal conductivity ($W\cdot m^{-1}\cdot K^{-1}$) or turbulence kinetic energy(J)
L	length (m)
$\dot{m}$	coolant mass flow rate ($g\cdot s^{-1}$)
n	the number of jet hole
P	total pressure or static pressure (Pa)
Q	the heat flow of the heating surface (W)
q	heat flux of the heat transfer surface ($W\cdot cm^{-2}$)
Re	Reynolds number
$T, \overline{T}$	temperature and the average temperature, respectively (K,°C)
u, v, w	velocity ($m\cdot s^{-1}$)
W	width (m)

Greek symbols

ρ	density ($kg\cdot m^{-3}$)
ε	dissipation rate of turbulence kinetic energy
λ_{eff}	effective thermal conductivity ($W\cdot m^{-1}\cdot K^{-1}$)
μ	dynamic viscosity (Pa·s)
η_t	eddy viscosity coefficient
$\sigma_\varepsilon, \sigma_k$	turbulent Prandtl numbers for k and ε

Subscript

$b, base$	the base area (smooth plate area)
$core$	the core region
f	average value of inlet and outlet
h	high heat flow region
$inlet, in$	the heat sink inlet or the jet hole inlet
jet	jet hole
l	low heat flow region
max	maximum value
min	minimum value
$outlet, out$	the heat sink outlet or the jet hole outlet
$pumping$	pump power consumption
s	solid domain
$t, total$	total heat transfer area (base plus fins)
w	the heat transfer surface

Abbreviations

SP	smooth plate
NP	non-uniform pin–fin plate
UP	uniform pin–fin plate
MP-SoCs	multi-processor system-on-chips
C-JIHS	conventional jet impingement heat sink
HT-JIHS	hotspot-targeted jet impingement heat sink

According to whether the jet space is limited, jet impingement can be divided into free jet and confined jet impingement. Due to the relatively simple structure of free jet impingement, scholars have carried out a lot of experimental research on free jet in the early stage. Donaldson et al. experimentally studied the behavior of free jet impinging on surfaces of several shapes at various impingement angles [22]. By analyzing the experimental data, they proposed a fitting relationship to approximately depict the impact of surface curvature on the stagnation point radial velocity gradient. In addition, they found that the heat transfer in the near stagnation point region with strong turbulence can be estimated by calculating the laminar heat transfer and applying the correction factor [23]. Dagan et al. investigated the heat transfer performance of jet arrays with four or nine free surface jets impinging on square 12.7×12.7 mm^2 heat sources. The experimental results show that the heat transfer coefficient was independent of the jet-to-target spacing in the range 3 mm$\leqslant z \leqslant$10 mm by using FC-77 and water as the coolants. However, the heat transfer coefficient in the stagnation region can be improved by decreasing the jet diameter with a given flow rate per heat source [24]. Not long before, Sorour et al. further studied the effects of jet-to-target spacing ratio ($z/d = 0.5, 1, 2, 4$ and 8) and Reynolds number on the heat transfer performance of free surface jet on a stainless-steel heated plate by using water - SiO_2 nanofluid. The experimental results show that the enhancement of average Nusselt number increases with the volume fraction and Reynolds number. However, the effect of jet-to-target spacing ratio is not significant [25].

However, to meet the requirement of compactness and miniaturization, the space of cooling device will be greatly limited. As a result, the confined submerged jet is more suitable for heat dissipation of electronic devices than free jet. In addition, some published works also shown that the heat transfer performance of confined submerged jet impingement is better than that of free jet impingement at the same conditions [26,27]. Kiper [28] is one of the earliest researchers to promote jet array impingement as a feasible cooling method for electronic devices heat dissipation. In the experiment of large area VLSI circuit with submerged liquid jet array cooling, it was found that the heat transfer coefficient was significantly higher than conventional liquid cooling technologies, e.g. immersion cooling and microchannel cooling, by scaling the jet array impingement cooling technology to small flow passage dimensions. In addition, Fabbri et al. [29] found that the pressure drops across the orifice needed to form the jet is not necessarily related to the heat transfer mechanisms at the impingement surface, which contrasts with other liquid cooling technologies such as single-phase or two-phase microchannel flow where the heat transfer and pressure drop are all interrelated. This desirable characteristic provides the possibility of optimizing the jet configuration to reduce pumping power while improving heat transfer performance. To achieve this purpose, a large quantity of numerical simulations and experiments have been carried out to study the influence of jet hole diameter, jet-to-jet spacing, jet-to-target spacing and enhanced surface type on heat transfer performance. Wang et al. studied the single jet and jet arrays by analytical and experimental methods, and the effects of jet hole diameter and the number of jet holes on cooling performance were investigated [30]. Subsequently, Wei et al. compared the heat transfer performance and resistance characteristics of single hole jet (2 mm diameter nozzle) and jet array (4×4 array with $500\mu m$ diameter) by using a high spatial resolution and programmable thermal test chip. The results indicate that the jet array impingement achieves a lower thermal resistance and a better temperature uniformity for the same flow rate compared to the single jet [31]. Sung et al. studied the heat transfer performance of three jet patterns, i.e. decreasing-jet-size, equal-jet-size and increasing-jet-size pattern (the jet hole diameter decreases or increases gradually along the flow direction), with HFE-7100 as working fluid through experiment and numerical simulations. The results show that the decreasing-jet-size pattern yields the highest convective heat transfer coefficients and lowest wall temperature, while the equal-jet-size pattern provides the best uniformity in wall temperature [17]. Womac et al. studied the effects of jet-to-jet spacing and jet-to-target spacing on heat transfer performance using water and FC-77 as working fluids, respectively. The

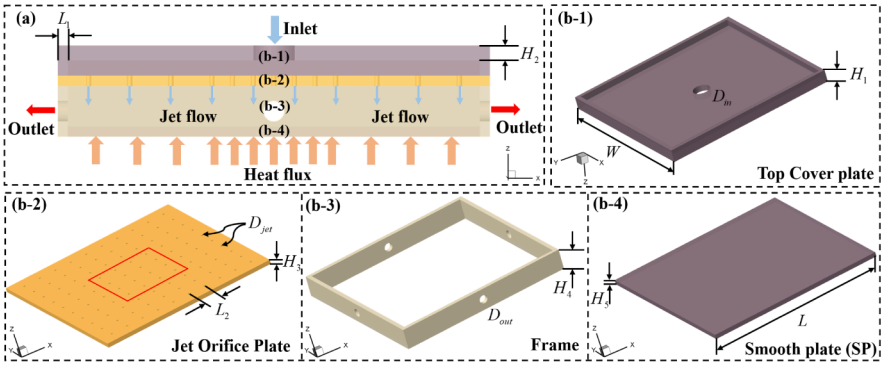

(I) Conventional jet impingement heat sink 3D model in (a) and 3D model diagram of each part in (b-1), (b-2), (b-3) and (b-4)

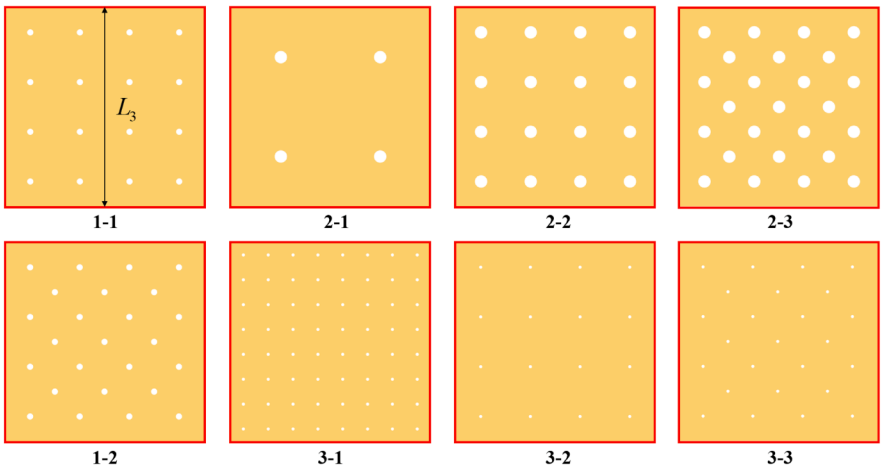

(II) Different arrangements of jet holes in the core region (The diameter of three different types of jet holes are 0.25mm, 0.5mm and 1mm respectively)

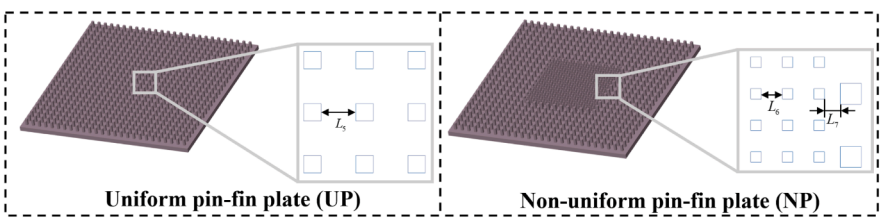

(III) 3D model diagram of uniform pin-fin plate and non-uniform pin-fin plate

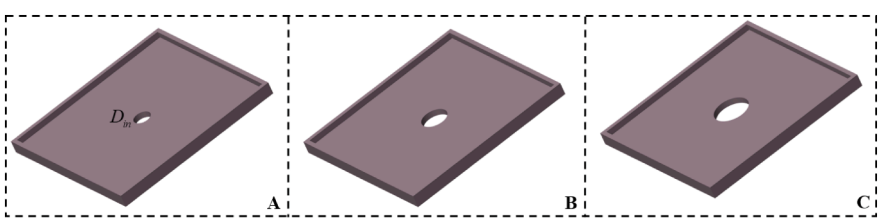

(IV) 3D model diagram of top cover plate with different inlet diameter ($D_{in-A} = 4\text{mm}$, $D_{in-B} = 6\text{mm}$, $D_{in-C} = 8\text{mm}$)

Fig. 1. Physical model of jet impingement heat sink.

Table 1
Geometrical parameters of C-JIHS and HT-JIHS [mm].

L	W	L_1	L_2	L_3	L_4	L_5	L_6
40	42	1	4	16	20	1	0.5
L_7	H_1	H_2	H_3,H_5	H_4	D_{inlet}	D_{jet}	D_{outlet}
0.375	3	1.5	1	3.5	4/6/8	0.25/0.5/1	2

results indicate that the average heat transfer coefficient was relatively intensive to jet-to-target spacing within the range $2 \leqslant H/d_n \leqslant 4$ [27]. Like in [27], Robinson et al. found the similar experimental phenomenon when exploring the effects of jet-to-jet spacing and jet-to-target spacing on heat transfer performance [26].

In order to further improve the heat transfer performance and solve the problem of lacking heat transfer area, some scholars propose to introduce enhanced structures on the impingement surface [32]. Besides increasing the total heat transfer area, the presence of the enhanced structure can potentially increase the heat transfer performance through flow mixing, boundary layer interruption and turbulent transport [33]. Sullivan et al. [34] is one of the earliest researchers to study the heat transfer performance of jet impingement on enhanced surface. They experimentally investigated the performance of smooth and enhanced spreader plates under submerged jet impingement. Compared with smooth spreader plate, the thermal resistance of enhanced spreader plate can be reduced by 60% with the largest jet diameter. Ndao et al. [33] experimentally investigated the single-phase stagnation point jet impingement heat transfer on smooth and micro pin–fin structures using water and R134a. The experiment results show that the heat transfer coefficient was significantly enhanced owing to the presence of micro pin fins on the impingement surface. Enhancement factor as high as 3.03 in the heat transfer coefficient was demonstrated. In addition, some scholars have also carried out simulation research on the performance of jet array impinging on the enhanced surface. Husain et al. [35] carried out a three-dimensional numerical simulation to study the effects of adding pillar structure on the thermal performance. Huang et al. [36–38] investigated the influence of dimple structure, introduced into the jet impingement surface, on flow and heat transfer characteristics by numerical simulation. The results show that the jet impingement heat sink with convex dimples exhibited the best cooling performance. In contrast to increasing heat transfer area, some scholars propose to reduce the contact thermal resistance and improve the cooling efficiency by processing the jet impingement cold plates directly on the chip through 3D printing or photolithography technology. Wei et al. investigated the thermal and hydraulic characterization of package level 3D printed direct liquid micro-jet array impingement cooling applied to the dual-chip module by means of experiments and numerical simulation. The results show that a very low thermal resistance of 0.26 cm^2K/W is measured at a cooler flow rate of 1000 ml/min for two heated chips while the heat flux is up to 300 W/cm^2 and the pressure drop is 0.09 bar [39]. Drummond et al. used photolithography to construct micro-channels imbedded directly into the heated substrate to reduce the parasitic thermal resistance due to contact and conduction resistance.

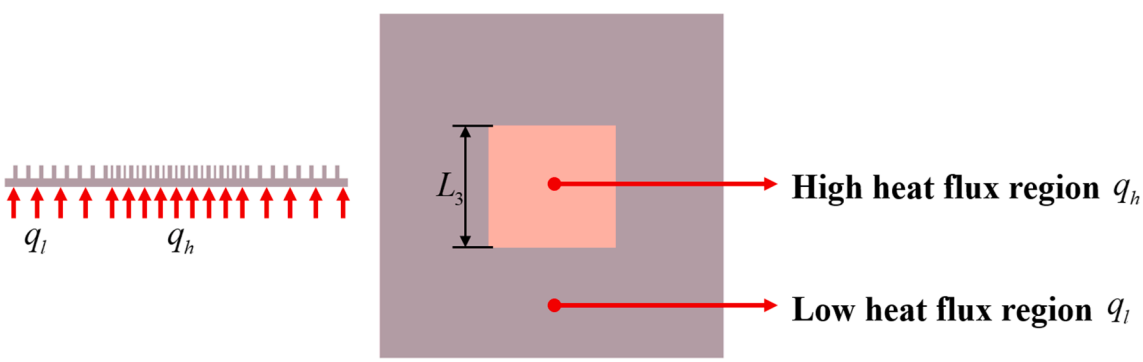

Fig. 2. Schematic diagram of heat flux distribution at the bottom of heat transfer plate.

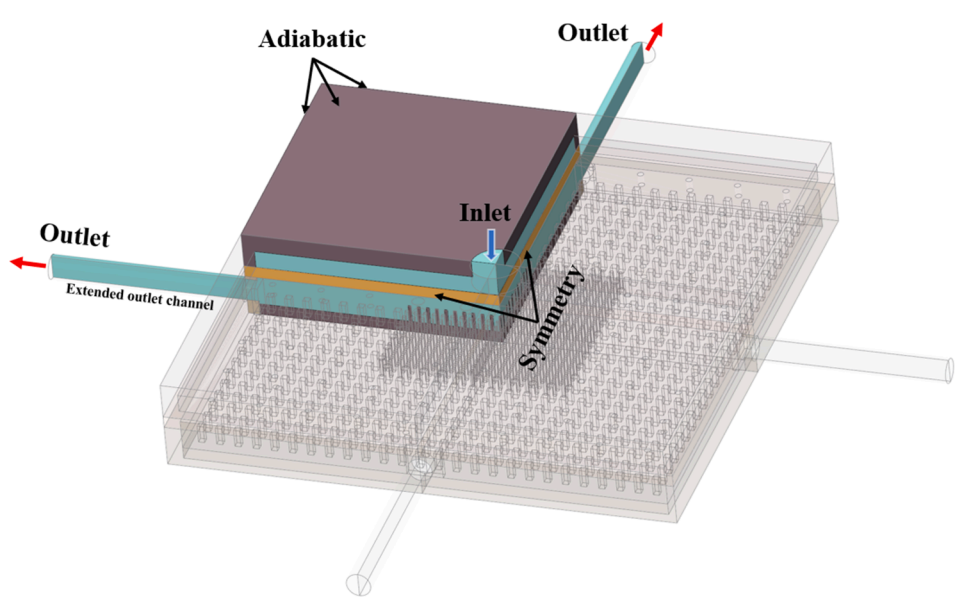

Fig. 3. Calculation model with boundary conditions.

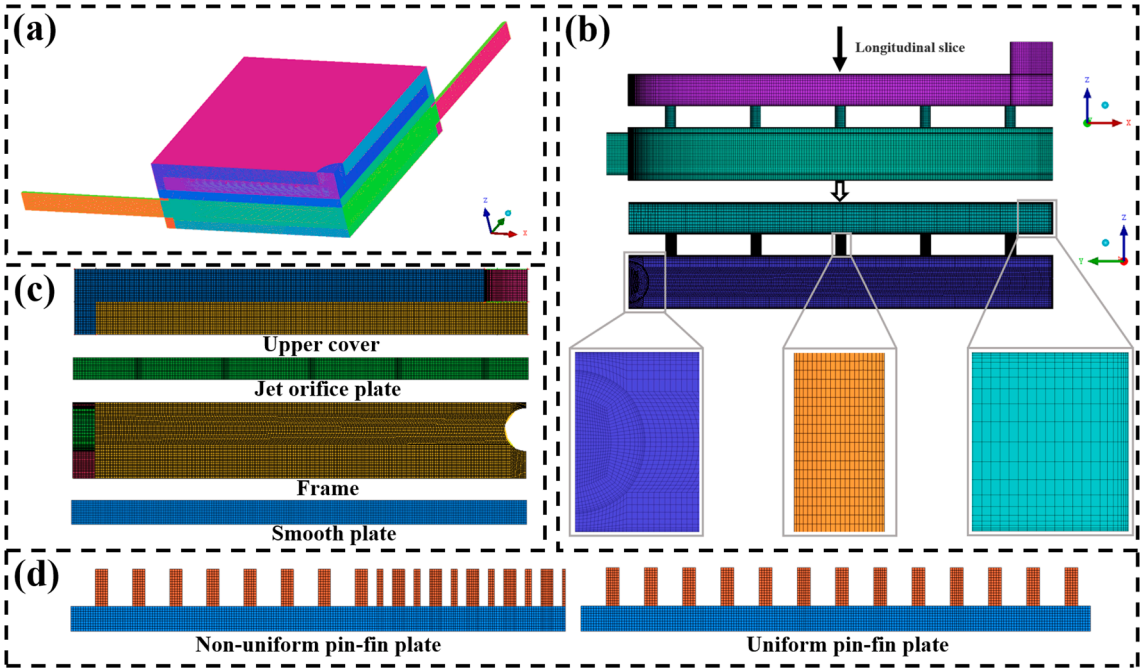

Fig. 4. The overall mesh in (a) and regional mesh of different part in (b), (c) and (d).

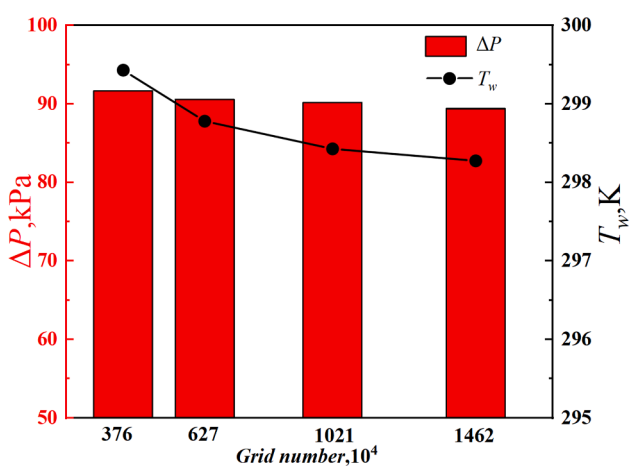

Fig. 5. Grid independence study.

Table 2
Grid independence information for all different heat transfer plates.

	Grid number	Average heat transfer surface temperature (K)	Relative error	Pressure drop (Pa)	Relative error
Smooth plate	3,760,070	299.43	0.39%	91,656	2.53%
	6,277,301	298.78	0.17%	90,557	1.3%
	10,215,975	298.42	0.05%	90,169	0.87%
	14,625,349	298.27	–	89,393	–
Uniform pin–fin plate	4,104,978	292.62	0.13%	92,244	0.52%
	6,250,100	292.69	0.15%	93,099	0.39%
	12,987,115	292.24	–	92,730	–
Non-uniform pin–fin plate	3,276,704	292.22	0.04%	92,345	0.58%
	6,822,578	291.99	0.04%	93,196	0.34%
	11,841,804	292.10	–	92,881	–

The experimental results show that the heat sink with 15 $\mu m \times 300$ μm channels can dissipate base heat fluxes up to 910 W/cm^2 at pressure drop of less than 162 kPa and chip temperature rise under 47 °C relative to the fluid inlet temperature [40].

From the above literature research, it can be found the submerged jet impingement cooling technology has better heat transfer performance and is suitable for the cooling of electronic devices. In addition, due to the pressure drop needed to form the jet is not necessarily related to the heat transfer mechanisms at the impact surface, the heat transfer performance can be dramatically improved while the pressure drop will not increase greatly by optimizing the structure parameters, e.g. jet hole diameter, jet-to-jet spacing, jet-to-target spacing and enhanced surface type. However, all these studies have considered only uniform heat flux distribution, which is not consistent with the practical situation and is not suitable for future multicore chip heat dissipation. When the conventional jet impingement heat sink (C-JIHS) is used to cool the electronic devices with non-uniform heat flux generation, two adverse consequence will be caused. First, the reliability problem. Due to the coolant distribution of C-JIHS is relatively uniform, when the hotspot (high heat flux region) temperature is cooled to a safe temperature, the temperature of low heat flux region is often significantly lower than that. The large temperature gradient will cause large gradient of thermal expansion, increasing thermal stresses between two different materials, especially for heterogeneous chips, reducing electronic reliability in the high temperature region and thus leading to differential aging [41]. Second, the pump power consumption problem. In order to ensure that the hotspot temperature is lower than the safe temperature, higher coolant volume requirement will increase the pumping power cost. Consequently, the C-JIHS will not be sufficient to address the cooling and energy efficiency requirement of future electronics with significant non-uniform heat generation.

In order to solve the contradiction between cooling performance and energy efficiency, a novel cooling concept targeted at hotspot is required. According to our literature research, some scholars have proposed to optimize the channel arrangement of the microchannel heat sink to deal with the heat dissipation problem in hotspot area [41–45], but the microchannel heat sink inherently has the disadvantage of large temperature and pressure drop gradient along the flow direction [11,17]. Compared with microchannel cooling, jet impingement cooling

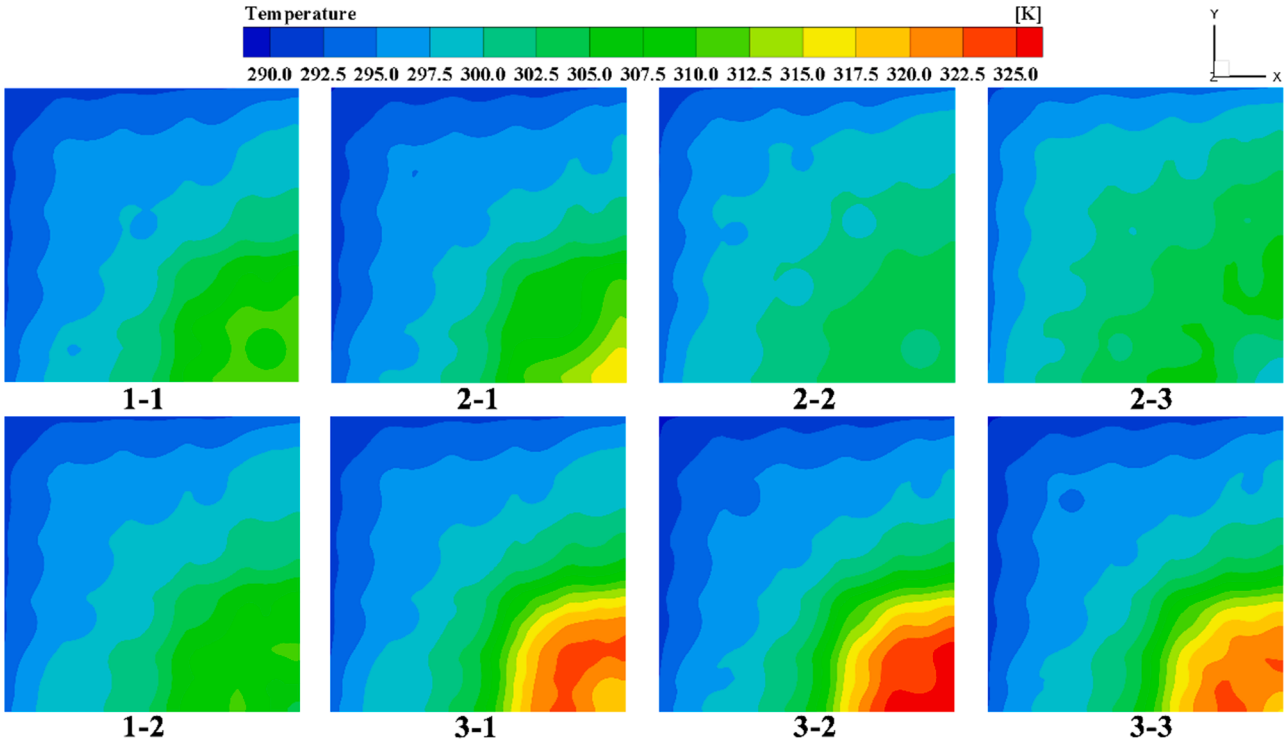

Fig. 6. The temperature distribution of smooth plate with different jet orifice plates (q_h = 100 W/cm^2,q_l = 50 W/cm^2,$\dot{m}$ = 25.08 g/s).

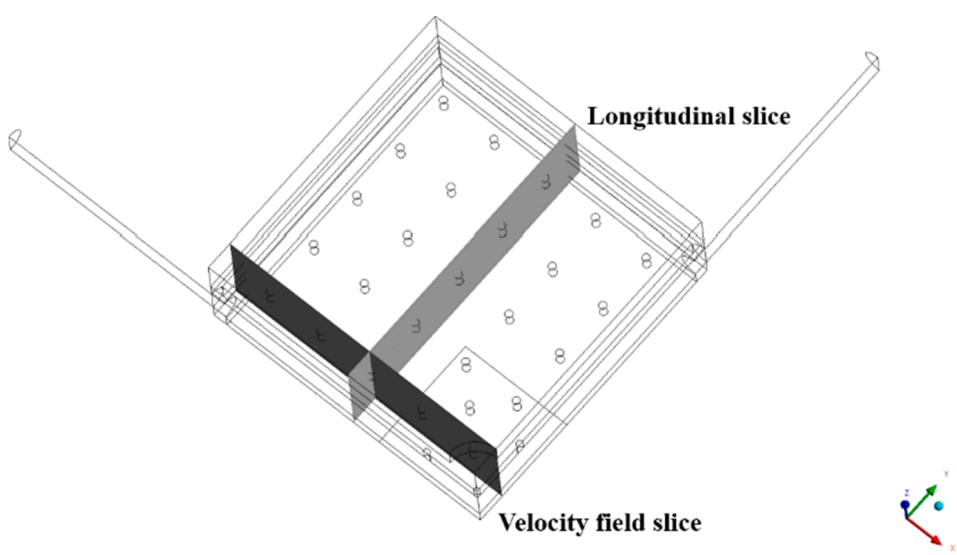

Fig. 7. Relative position of slice in heat sink.

Table 3
The detailed values of numerical results [K], [W·cm $^{-2}$·K $^{-1}$].

	1–1	1–2	2–1	2–2	2–3	3–1	3–2	3–3
$\overline{T}_w$	298.78	299.02	298.59	298.76	300.1	301.17	300.67	300.4
$\overline{T}_{w,core}$	308.63	307.92	309.16	303.38	304.06	318.81	319.76	317.77
ΔT	21.8	20.07	27.53	14.1	14.52	33.32	38.96	33.74
$\overline{h}_b$	3.42	3.35	3.46	3.37	3.07	2.93	3.03	3.08
$\overline{h}_{b,core}$	3.17	3.32	3.02	4.69	4.65	1.68	1.55	1.71

has better resistance performance and the jet stagnation zone has an extremely high heat transfer coefficient [18]. However, the application of jet impingement cooling to solve the heat dissipation problem of non-uniform heat flux is relatively less. In this work, we construct hotspot-targeted jet impingement numerical models to investigate the effects of structural parameters, i.e. jet hole diameter and arrangement,

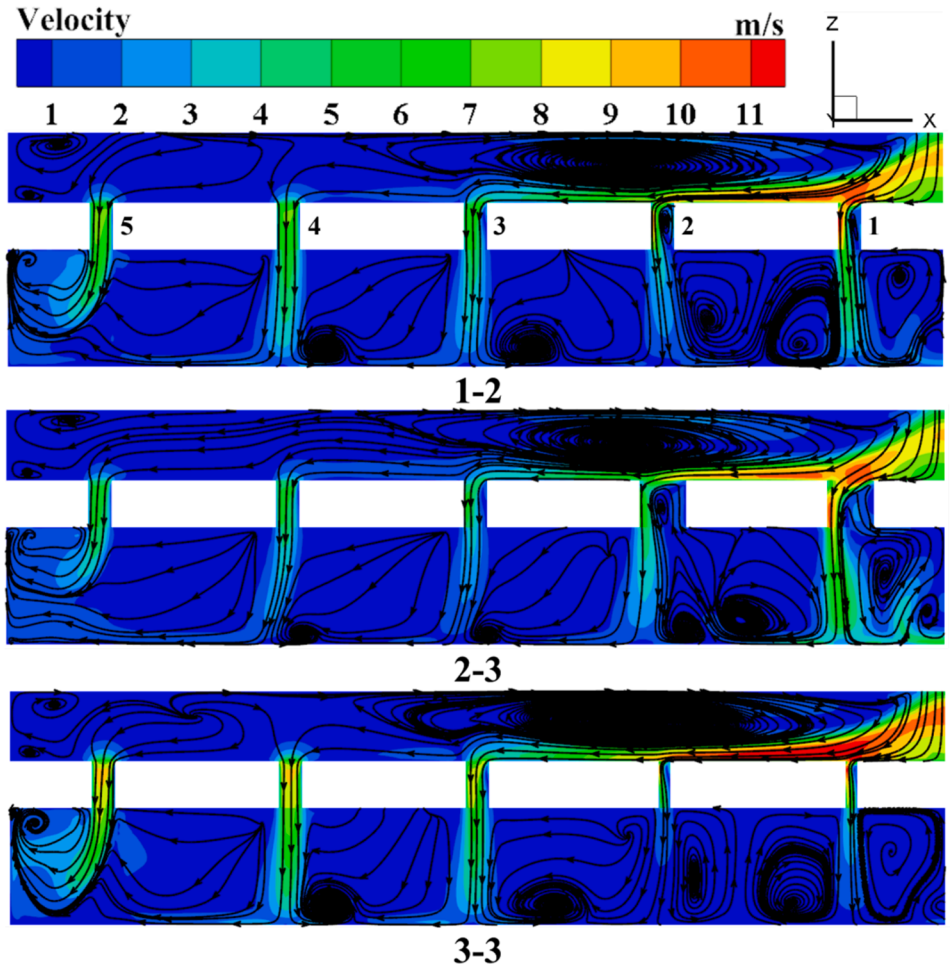

Fig. 8. Streamlines and contour of velocity magnitude for different jet orifice plates.

impingement surface type (smooth plate, uniform pin–fin plate and non-uniform pin–fin plate), on heat transfer and resistance characteristics. Additionally, to further improve the resistance performance of hotspot-targeted jet impingement heat sink (HT-JIHS), the influence of different inlet areas was also investigated.

2. Numerical methodology

2.1. Geometric model and variable settings

Fig. 1(I) shows the three-dimensional model of C-JIHS, being taken as reference in the numerical simulation, which consists of four parts: the top cover plate, the jet orifice plate, the frame and the smooth target plate. Table 1 lists the main dimensions corresponding to each part. The overall structure and size of HT-JIHS are basically the same as C-JIHS, except for the specific structure of jet orifice plate and heat transfer plate. In general, the coolant flows in from the inlet, stagnates in the stagnation chamber, and then is forced across the jet nozzle plate to wash against the heat transfer plate and moves radially outwards. Different from the previous studies, the heat flux distribution at the bottom of the heat transfer plate is uneven. As shown in Fig. 2 and Fig. 1(I), the middle part of the heat transfer plate is the high heat flux region (core region), and the rest is the low heat flux region (edge region). Although the research in this work is for chips with only one hotspot area, the design strategy can be directly extended to the heat sink design of multi-core hotspot area and the verification of multi-core hotspot heat dissipation is shown in the appendix.

In order to achieve a uniform temperature distribution under the non-uniform heat flux generation, the arrangement of the jet holes and pin fins is investigated. As shown in Fig. 1(II), there are eight kinds of jet hole arrangements in the core region, i.e. the red wire frame in Fig. 1(I)(b-2), among which the jet hole diameter in the edge region is all 0.5 mm. The jet hole arrangement of 2–1 and 3–1 have the same jet hole area as 1–1, but the jet hole diameter is different in the core region, as shown in the marked area in the figure. Additionally, to further explore the influence of jet hole numbers on heat transfer characteristics under the same jet hole diameter, the arrangement models of 1–2, 2–2, 2–3, 3–2 and 3–3 are investigated.

Fig. 1(III) shows the different arrangements of pin fins on the target surface. For uniform pin–fin plate, the sizes of the pin fins are the same, with length, width and height of 0.5 mm, 0.5 mm and 1.5 mm, respectively. To enhance the heat transfer performance in the core region, the pin fins with smaller sizes are used for non-uniform pin–fin plate, which have a larger specific surface area compared with thick pin fins. The length, width and height of the pin fins in the core region are 0.25 mm, 0.25 mm and 1.5 mm, respectively, and the sizes of pin fins in edge region are the same as that of uniform pin–fin plate. In addition, the effect of inlet area of the heat sink on the heat transfer and pressure drop characteristics is also investigated. Fig. 1(IV) displays the three different diameters of the heat sink inlet, type A, B, and C, respectively. It should be noted that a stagnation chamber will be formed after the top cover plate and the jet orifice plate are tightly fitted, which is used for fluid buffering and distribution.

In the numerical simulation, the mass flow rate of coolant into the heat sink is controlled by changing the inlet velocity, and the corresponding *Re* ranges from 600 to 2900. Various structural parameters

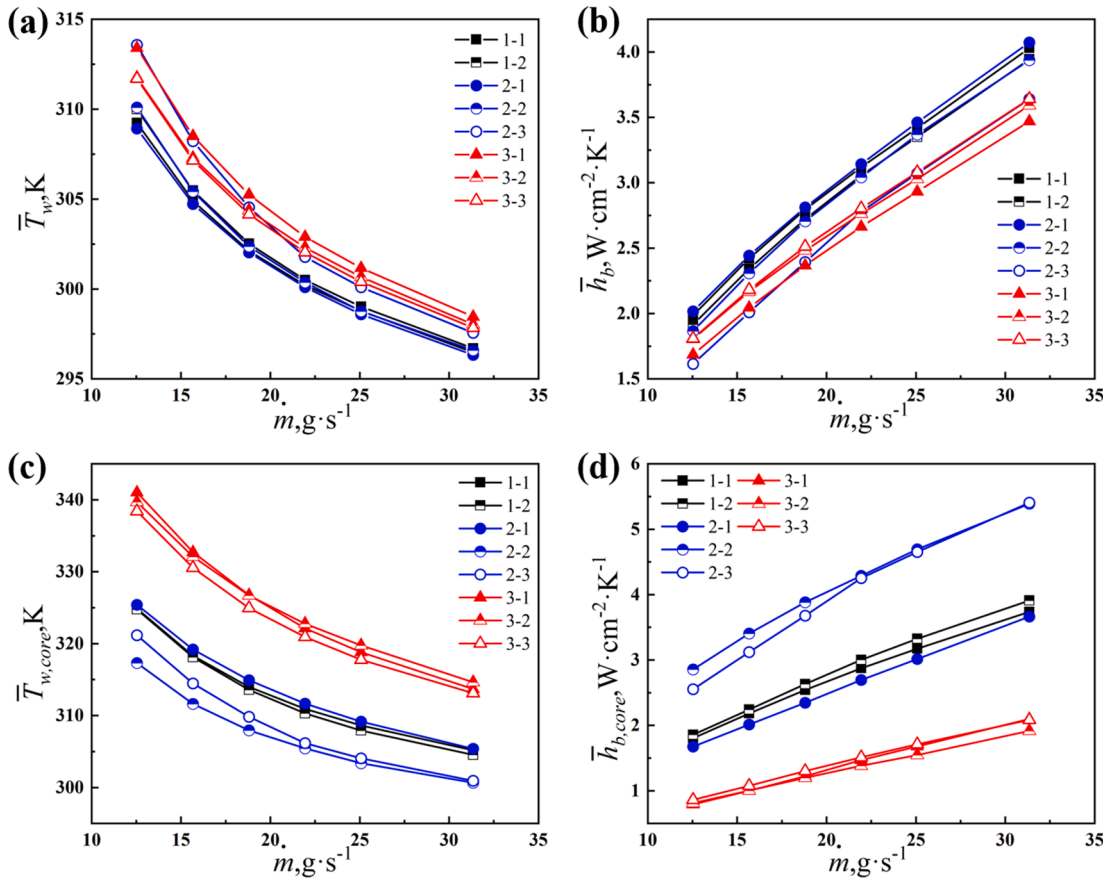

Fig. 9. The average temperature and heat transfer coefficient of the whole heat transfer surface (a)(b) and the core region (c)(d) under different mass flow rates (q_h = 100 W/cm^2,q_l = 50 W/cm^2).

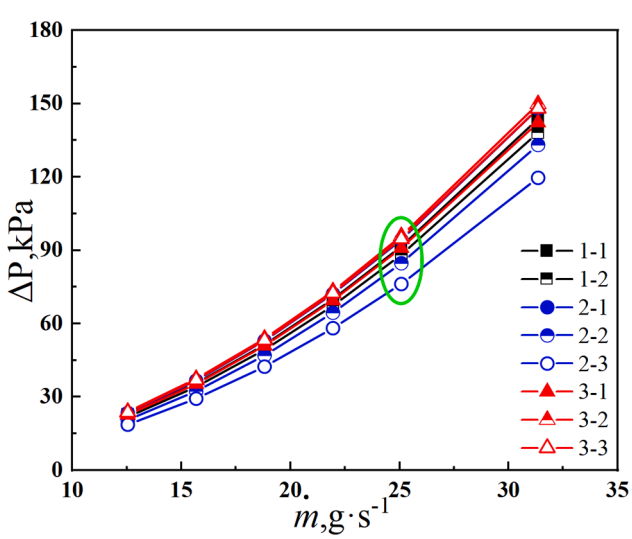

Fig. 10. Total pressure drop with different mass flow rates.

including jet hole diameter and number, inlet area and impingement surface type are considered.

The Reynolds number is defined as:

$$Re = \frac{\rho u_{jet} D_{jet}}{\mu} \tag{1}$$

$$D_{jet} = \frac{\sum_{i=1}^{n} D_{jet,i}}{n} \tag{2}$$

where u_{jet} is the average velocity of jet hole, $D_{jet,i}$ is the diameter of jet hole, n is the number of jet hole and μ is the dynamic viscosity coefficient of fluid.

The heat flux is given by:

$$q_{total} = \frac{Q}{A_{total}} \tag{3}$$

$$q_{base} = \frac{Q}{A_{base}} \tag{4}$$

where Q is the heating power of the heating surface, A_{total} is the total heat transfer area (base plus fins) and A_{base} is the base area (smooth plate area).

The average heat transfer coefficient is then given by:

$$\overline{h}_t = \frac{q_{total}}{T_w - T_f} \tag{5}$$

$$\overline{h}_b = \frac{q_{base}}{T_w - T_f} \tag{6}$$

where T_w is the average temperature of the heat transfer surface and T_f is the average temperature of the heat sink inlet and outlet.

The pressure drop is defined as:

$$\Delta P = P_{inlet} - P_{outlet} \tag{7}$$

$$\Delta P_1 = P_{inlet} - P_{jetin} \tag{8}$$

$$\Delta P_2 = P_{jetin} - P_{jetout} \tag{9}$$

$$\Delta P_3 = P_{jetout} - P_{outlet} \tag{10}$$

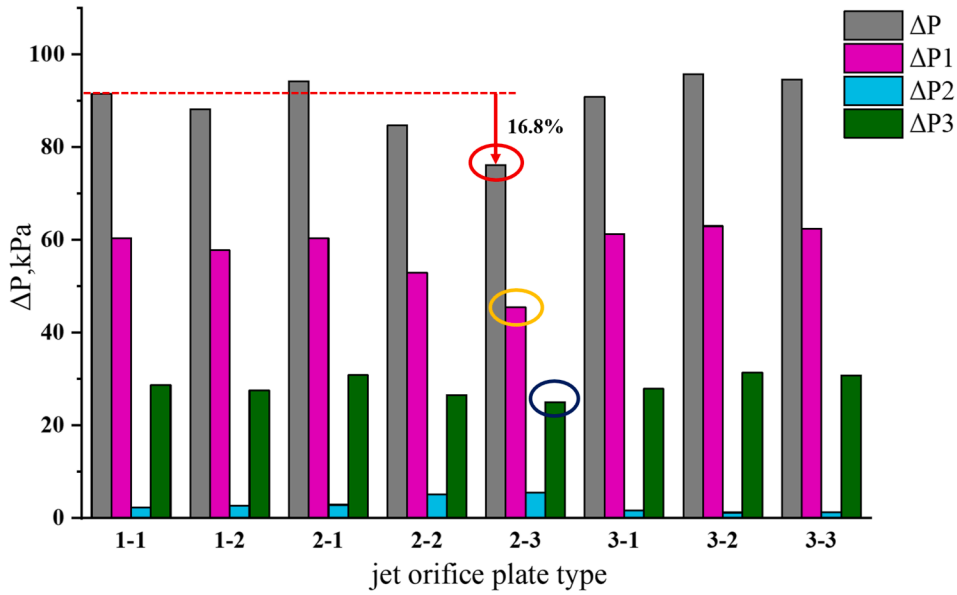

Fig. 11. Pressure drop in jet impingement heat sink for different jet orifice plates.

where P_{inlet} is the mass-weighted average total pressure of the heat sink inlet, P_{out} is the mass-weighted average total pressure of the heat sink outlet, P_{jetin} is the mass-weighted average total pressure of the jet inlet and P_{jetout} is the mass-weighted average total pressure of the jet outlet.

The pump power consumption is defined as:

$$\dot{W}_{pumping} = \Delta P \frac{\dot{m}}{\rho} \tag{11}$$

where $\dot{m}$ is the mass flow rate of the heat sink and ρ is the density of water.

2.2. Numerical calculation model and boundary conditions

According to our previous experimental and numerical studies [46], it is found that the RNG $k-\varepsilon$ turbulence model can better simulate the jet impingement heat sink with ribs on the heat transfer plate in the middle-Reynolds-number range ($500 < Re < 2000$). In addition, the two-equation $k-\varepsilon$ turbulence model is also widely used and validated in some relevant published works [17,36,47–49]. Therefore, the RNG $k-\varepsilon$ model with moderate computational cost and acceptable accuracy is finally selected for all the numerical calculations.

To simplify the calculation, the flow is assumed to be steady, incompressible and continuous. The commercial software (Fluent 16.0) is used to compute fluid flow and heat transfer characteristics of the hybrid cooling module. The detail information about governing equations and convergence conditions are shown in the appendix.

As for the boundary conditions, the inlet boundary is set as velocity inlet at a temperature of 283 K. The outlet is pressure outlet, and the gage pressure is 0 Pa. The bottom heating surface is set to the constant heat flux, including a high heat flux region (q_h) and a low heat flux region (q_l). Three kinds of power map, i.e. $q_h = 100\text{W/cm}^2$ and $q_l = 50\text{W/cm}^2$, $q_h = 150\text{W/cm}^2$ and $q_l = 25\text{W/cm}^2$, $q_h = 300\text{W/cm}^2$ and $q_l = 25\text{W/cm}^2$, are calculated. Only heat transfer is considered in the solid domain, the solid–liquid interface is set to no-slip and interface coupled, and the rest of the walls are adiabatic.

2.3. Meshing strategy

Considering the symmetry of the entire model in the direction of X and Y axis, one quarter of the whole model is selected as the calculation model, as shown in Fig. 3. In addition, to eliminate the effects of backflow and improve the calculation accuracy, the outlet exit section is extended by 8 D_{outlet}. Fig. 4 depicts the overall mesh of the heat sink with smooth plate and the hexahedral mesh of each part is generated by commercial software (ICEM 16.0) since the complexity of the entire model, different parts of the model are divided into blocks and the solid–liquid contact surface adopts coupled interface. To meet the y+ requirements of the enhanced wall treatment and ensure the accuracy of the numerical calculation, the solid–liquid contact surface has been refined and the grid height of the first layer is set to 0.01 mm, and the growth factor is set to 1.3. Fig. 4 (b) depicts the grid of fluid region inside the heat sink without outlet extension. By slicing the grid longitudinally, the zoom-in views of grid in the near wall region and the jet hole region can be observed and the slice position is shown in Fig. 7. More details about the meshing strategy can be found in our previous studies [46].

In the process of grid independence verification, the total number of grids is changed by adjusting the maximum grid size while maintaining the same refined conditions of the near-wall region. Fig. 5 shows the comparison of average heat transfer surface temperature and pressure drop for four different grid numbers of heat sink with smooth plate. The detailed temperature and pressure drop values are depicted in Table 2. Visibly, the precision is maintained and the relative error of average heat transfer surface temperature is close to 0.1% when the grid number reaches 6.27 million, which has met the accuracy requirement, and is consequently adopted in the subsequent calculation. Similarly, the grid number of 6,250,100 and 6,822,578 are selected to calculated the heat sink with uniform pin–fin plate and non-uniform pin–fin plate, respectively. In addition, the same meshing strategy and refinement conditions are adopted when the structural parameters of the heat sink change.

3. Results and discussion

3.1. Effect of jet hole diameter and arrangement

3.1.1. Heat transfer characteristics

As shown in Fig. 6, the temperature distribution of smooth plate under different jet orifice plates are obtained by numerical simulation. The label of the figure corresponds to the jet orifice plate type and the detailed temperature values of the heat transfer surface are illustrated in Table 3. It can be noticed that for eight kinds of jet orifice plates, the temperature of the core region is higher than that of the edge region, especially for 3–1, 3–2 and 3–3. When the arrangement of the jet holes is

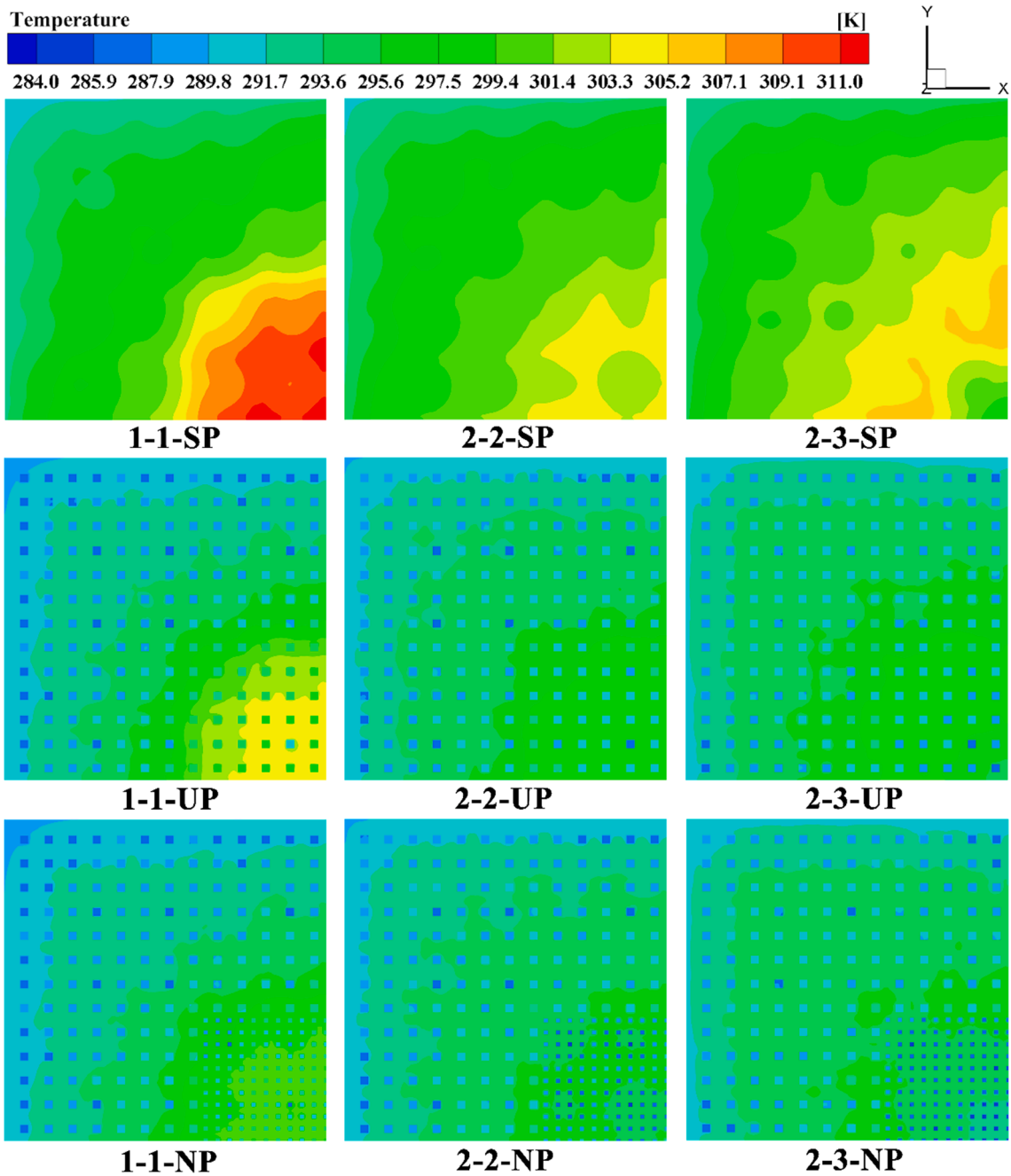

Fig. 12. The temperature contour map of three different impingement surface types (q_h = 100 W/cm^2,q_l = 50 W/cm^2,$\dot{m}$ = 25.08 g/s).

Table 4
The detailed numerical values for different target plates [K], [W·cm^{-2}·K^{-1}].

	T_{max}	T_{min}	ΔT	$\overline{T}_w$	$\overline{h}_b$
1–1-SP	311.97	290.17	21.8	298.78	3.95
2–2-SP	305	290.9	14.1	298.76	3.69
2–3-SP	306.41	291.89	14.52	300.1	3.63
1–1-UP	304.9	286.6	18.3	292.7	6.75
2–2-UP	299.2	287.18	12.02	292.25	7.12
2–3-UP	299.14	287.38	11.76	292.64	6.8
1–1-NP	301.27	286.47	14.8	292.99	7.36
2–2-NP	296.69	284.54	12.15	291.4	7.95
2–3-NP	296.69	284.06	12.63	291.63	7.71

the same, e.g. 1–2, 2–3 and 3–3, the smaller the diameter of the jet holes in the core region is, the higher the temperature of the heat transfer surface in the core region will be. In addition, even if the total jet hole area in the core region is the same, e.g. 1–1, 2–1 and 3–1, the temperature is relatively higher when the smaller jet hole diameter is used in the core region. By comparing the detailed temperature values of the heat transfer surface in Table 3, jet orifice plate 2–2 corresponds to the lowest $\overline{T}_{w,core}$(average temperature in the core region) and ΔT (the difference between the highest temperature and the lowest temperature of the heat transfer surface), which indicates that there is an optimal jet hole number in the core region.

Fig. 8 shows the streamlines and contour of velocity magnitude for three different jet orifice plates with the same jet hole arrangement and different jet hole diameters, i.e. 1–2, 2–3 and 3–3, at the mass flow rate of 25.08 g/s, for which the jet holes are numbered 1–5. The relative

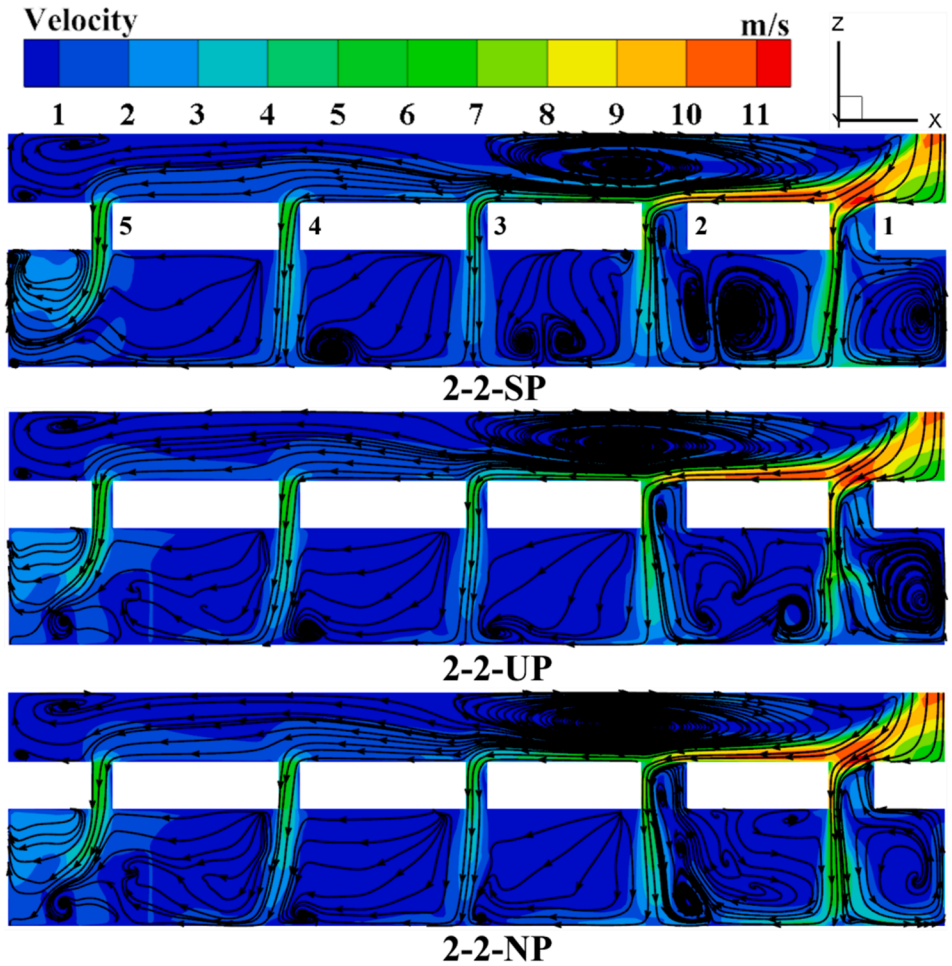

Fig. 13. Streamlines and contour of velocity magnitude for three different heat transfer plate.

position of velocity field slice is shown in Fig. 7. It should be noted that since the one quarter of the whole model is selected as the calculation region, the corresponding mass flow rate is one quarter of the total mass flow rate of the whole model. Observing Fig. 8, it is noteworthy that a high-speed horizontal cross flow is formed in the stagnation chamber after the inlet fluid impacts the jet orifice plate. When the jet hole diameter in the core area is small, for 3–3, the wall flow is approximately formed above the jet hole due to the high horizontal velocity, and less fluid passes through the jet hole. This results in poor convective heat transfer on core region of the heat transfer surface. On the contrary, more fluid flows out of the jet hole and scours the target surface vertically with larger jet hole diameter in the core region. As shown in Fig. 6, the core area of 2–2 and 2–3 with larger jet hole diameter has the lower and more uniform temperature distribution. Since our work only studied three different jet hole diameters, it can be inferred from previous literature studies that continuing to increase the jet hole diameter may lead to deterioration of heat transfer [50].

Additionally, when more fluid flows out from the jet hole in the core area, the more obvious the "drift phenomenon" caused by horizontal crossflow, which can be seen clearly in Fig. 8. Obvious differences of the streamlines for jet No. 1–4 are revealed between 2 and 3 and the other two cases. For 1–2 and 3–3, a pair of relatively symmetrical vortices were generated between jet No.1–2 and a separate vortex was generated below jet No.3 and No.4, while the vortices in 2–3 deflected to the downstream obviously and shrunk to a smaller scale owing to the severer crossflow. However, different from the uneven temperature distribution caused by the horizontal crossflow in previous studies [17,35,36], the side effect of horizontal crossflow makes the temperature distribution of the heat transfer surface tend to be uniform in our research.

Fig. 9 presents the variation of surface average temperature and convective heat transfer coefficient with mass flow rate for eight kinds of jet orifice plate within the mass flow rate range of 12.5–31.3 g/s. Observing Fig. 9(a), it can be noticed that when the jet hole diameter in the core region is 0.5 mm, i.e. 1–1 and 1–2, changing the number of jet holes in the core region, the average temperature of the heat transfer surface ($\overline{T}_w$) changes little, and the differences gradually decrease with larger $\dot{m}$. In addition, when the jet hole diameter is 0.25 mm in the core region, the same change rules are observed. However, for the case that the jet hole diameter in the core region is 1 mm, the number of jet holes has a great influence on the average temperature of the heat transfer surface. When the mass flow rate is small, the $\overline{T}_w$ of 2–3 is about 4°C higher than that of 2–2 and 2–1. In view of the above phenomenon, we speculate the increase of the jet hole numbers in the core region leads to more fluid cooling of the core region, which is conductive to the decrease of $\overline{T}_w$. Nevertheless, this also leads to the reduction of cooling fluid in the edge region and the heat transfer effect will deteriorate, which is conductive to the increase of $\overline{T}_w$. Therefore, increasing the jet hole area to enhance the heat transfer in the core region will cause the heat transfer deterioration in the edge region, which may lead to an increase in the average temperature of the heat transfer surface. In addition, according to the previous velocity field analysis, it is known that the larger the jet hole diameter is, the easier the fluid flows out of the jet hole. Therefore, for the case with large jet hole diameter, i.e. 2–1, 2–2 and 2–3, the change of the jet hole number has a greater influence on the variation of $\overline{T}_w$.

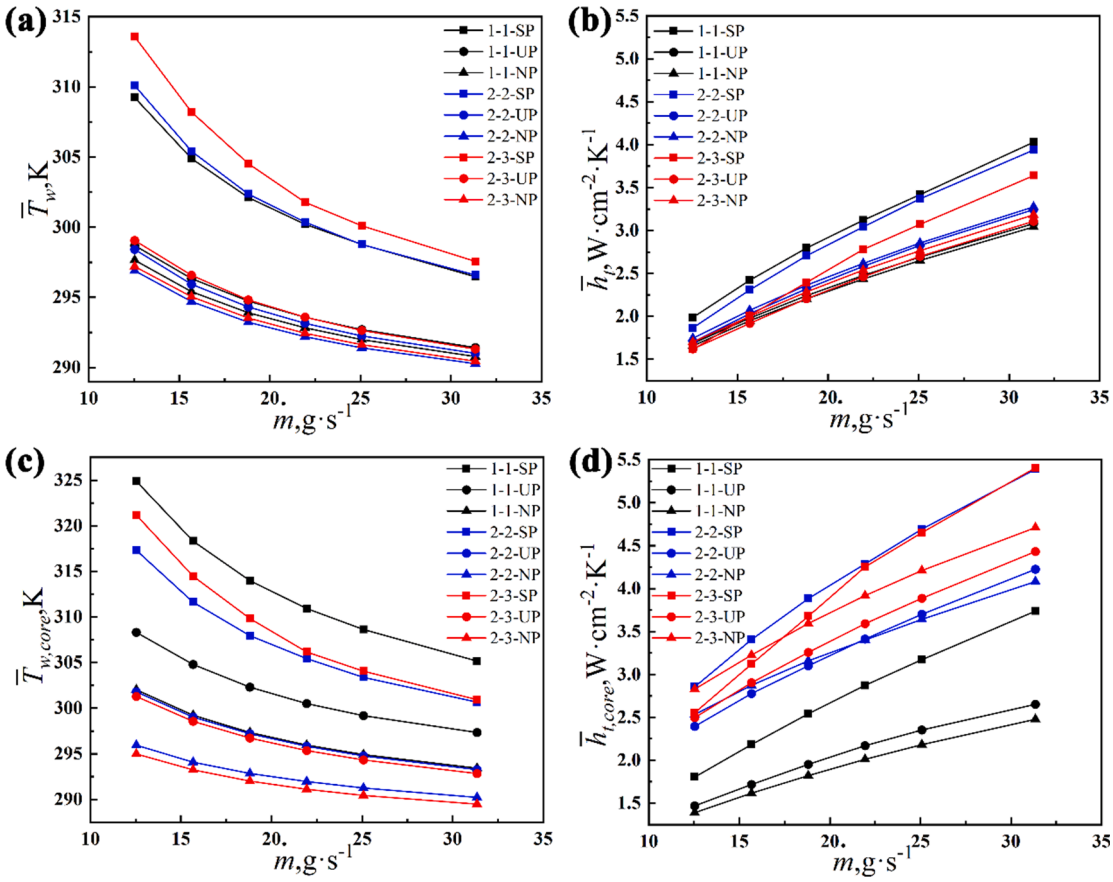

Fig. 14. The average temperature and heat transfer coefficient of the whole heat transfer surface (a)(b) and the core region of the heat transfer surface (c)(d) under different mass flow rates (q_h = 100 W/cm^2,q_l = 50 W/cm^2).

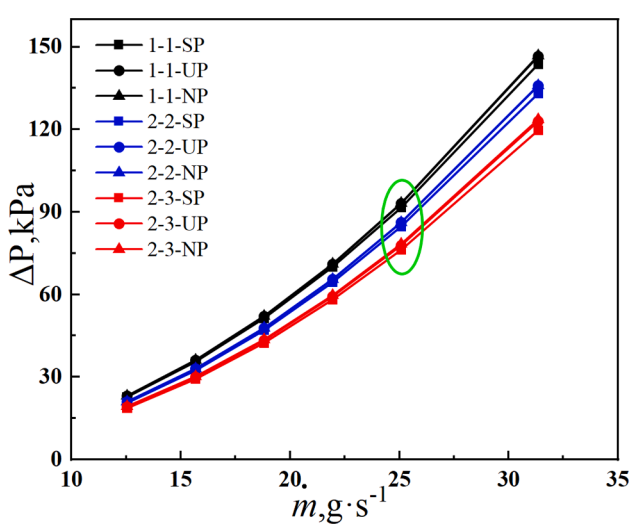

Fig. 15. Total pressure drop of heat sink with different heat transfer plates.

As shown in Fig. 9(c) and (d), similar to the variations trend of $\overline{T}_w$ and $\overline{h}_b$, when the jet hole diameter is 0.25 mm or 0.5 mm in the core region, changing the number of jet holes has little effect on $\overline{T}_{w,core}$ and $\overline{h}_{b,core}$ (average heat transfer coefficient in the core region). In addition, among the eight kinds of jet orifice plates, the 2–2 type jet orifice plate has the best heat transfer performance in the core region, while the 3–1, 3–2 and 3–3 type jet orifice plates have the worst heat transfer performance. Compared with the traditional jet orifice plate 1–1, the $\overline{T}_{w,core}$ of 2–2 is lower and the differences are close to 10°C when the mass flow rate is small. With the increase of mass flow rate, the temperature differences between different jet orifice plates decrease gradually. As for the average heat transfer coefficient in the core region, with the increase of mass flow rate, the heat transfer coefficient increases, and 2–2 and 2–3 type jet orifice plate have the highest heat transfer coefficient in core region. Moreover, when the mass flow rate is small, the $\overline{h}_{b,core}$ of 2–2 is slightly higher than that of 2–3.

3.1.2. Pressure drop characteristics

Fig. 10 demonstrates the variation of total pressure drop with mass flow rate for eight kinds of jet orifice plates. Notably, for eight kinds of jet orifice plates, the total pressure drop of the heat sink increases with larger mass flow rate. When the mass flow rate is small, the total pressure drops corresponding to eight kinds of heat sinks have little differences. Among eight kinds of jet orifice plates, the total pressure drop of 2–3 is the lowest and that of 3–2 is the highest. In order to further analyze the composition of pressure drop and investigate the influence of different jet orifice plates, a detailed analysis is carried out when the mass flow rate is 25.08 g/s, as shown in Fig. 11. Generally, the total pressure drop of heat sink is mainly composed of three part: ΔP_1, ΔP_2 and ΔP_3. ΔP_1 is the pressure loss of fluid from the inlet of heat sink to the

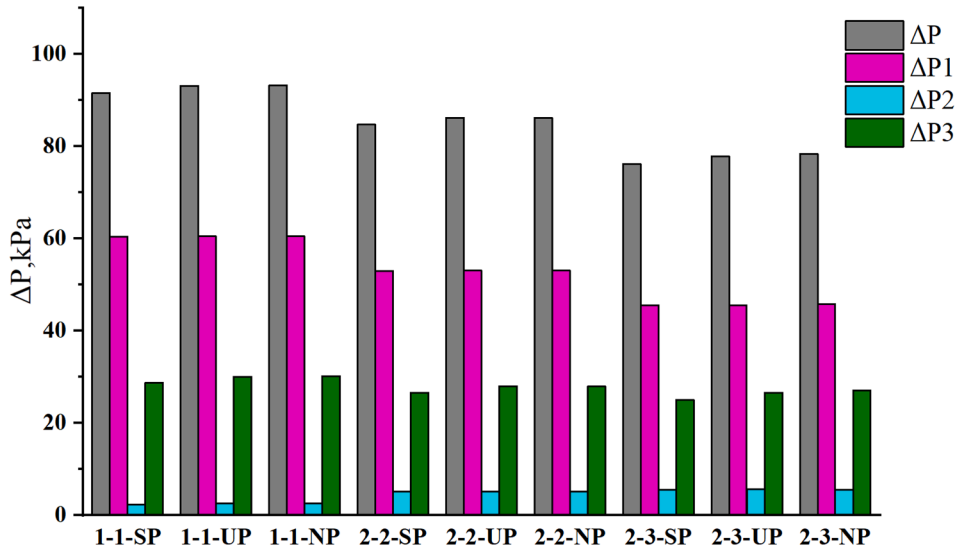

Fig. 16. Pressure drop in jet impingement heat sink with different heat transfer plates.

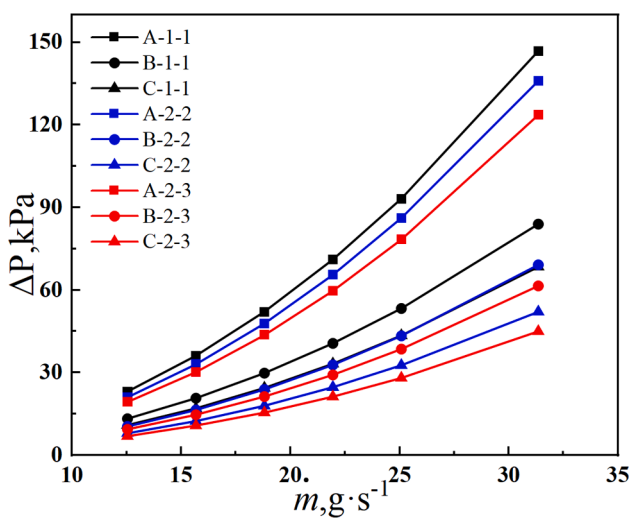

Fig. 17. Total pressure drop of three different heat sink inlet diameters.

entrance of jet hole, ΔP_2 is the pressure loss of fluid after flowing through the jet hole and ΔP_3 is the pressure loss of fluid from the outlet of jet hole to the outlet of heat sink. For all calculated cases, it can be noticed that ΔP_1 and ΔP_3 account for a large proportion of the total heat sink pressure drop, while ΔP_2 accounts for a small proportion, which is similar to the experimental study by Fabbri et al. [29]. In addition, compared with traditional jet hole arrangement 1–1, the total pressure drop of the heat sink with 2–3 type jet orifice plate decreases by 16.8%, which is mainly reflected in the decrease of ΔP_1 and ΔP_3. As can be seen from the previous velocity field analysis, high speed horizontal cross-flow will be formed in the stagnation chamber after the inlet fluid impacts the jet orifice plate, which will lead to large impact loss and resistance loss along the chamber. For 2–3 type jet orifice plate, the jet hole area in the core region is the largest, hence most of the fluid will move a shorter distance and flow out of the jet hole, which reduces the pressure loss along the chamber and leads to a smaller ΔP_1. Moreover, with the increase of jet hole area in the core region, ΔP_3 decreases gradually. This is consistent with the study by Sung [17] that when the decreasing-jet-size pattern (the closer to the heat sink outlet, the smaller the diameter of jet hole) is used, more fluid flows from the upstream jet hole. At this time, the velocity of the jet hole near the outlet decreases, which will not cause fluid blockage at the outlet of the heat sink and the resistance performance is better.

3.2. Effect of impingement surface type

3.2.1. Heat transfer characteristics

According to previous numerical results, the jet orifice plates 2–2 and 2–3 with the best heat transfer performance and resistance performance are selected to further investigate the effects of impingement surface type on heat transfer performance, and the traditional jet orifice plate 1–1 is taken as reference. Fig. 12 presents the temperature contour map for three different impingement surface types: smooth plate (SP), uniform pin–fin plate (UP) and non-uniform pin–fin plate (NP), and the detailed temperature values can be found in Table 4. Evidently, compared with the smooth plate, the introduction of pin–fin arrays can dramatically enhance the uniformity of the heat transfer surface temperature and lower the temperature in the core region. For smooth plate, the traditional jet orifice plate 1–1 corresponds to the worst heat transfer performance with the highest temperature in the core region, while the jet orifice plates 2–2 and 2–3 achieve a more uniform temperature distribution by altering the mass flow distribution. When the uniform pin–fin arrays are introduced to the target plate, the maximum temperature decreases significantly for the three kinds of jet orifice plates, and the average heat transfer coefficient of the target surface increases near 1.5 times. However, compared with 2–2-UP and 2–3-UP, the temperature of the core region for 1–1-UP is still significantly higher than that in the edge region. For 2–2-UP and 2–3-UP, it can be found that temperature distribution is relatively uniform and the temperature in the core region is basically the same as that in the edge region. In addition, by observing the detailed temperature values, it is worth noting that the difference between the maximum temperature and the minimum temperature is only about 11°C when the heat flux difference is 50 W/cm^2. When the non-uniform pin–fin arrays are introduced to the

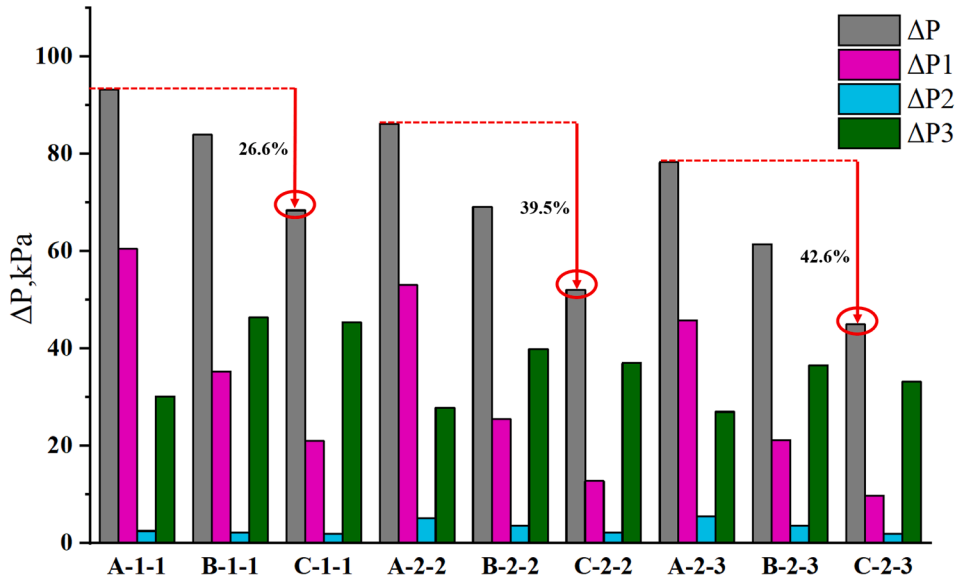

Fig. 18. Pressure drop in jet impingement heat sink with different inlet diameters.

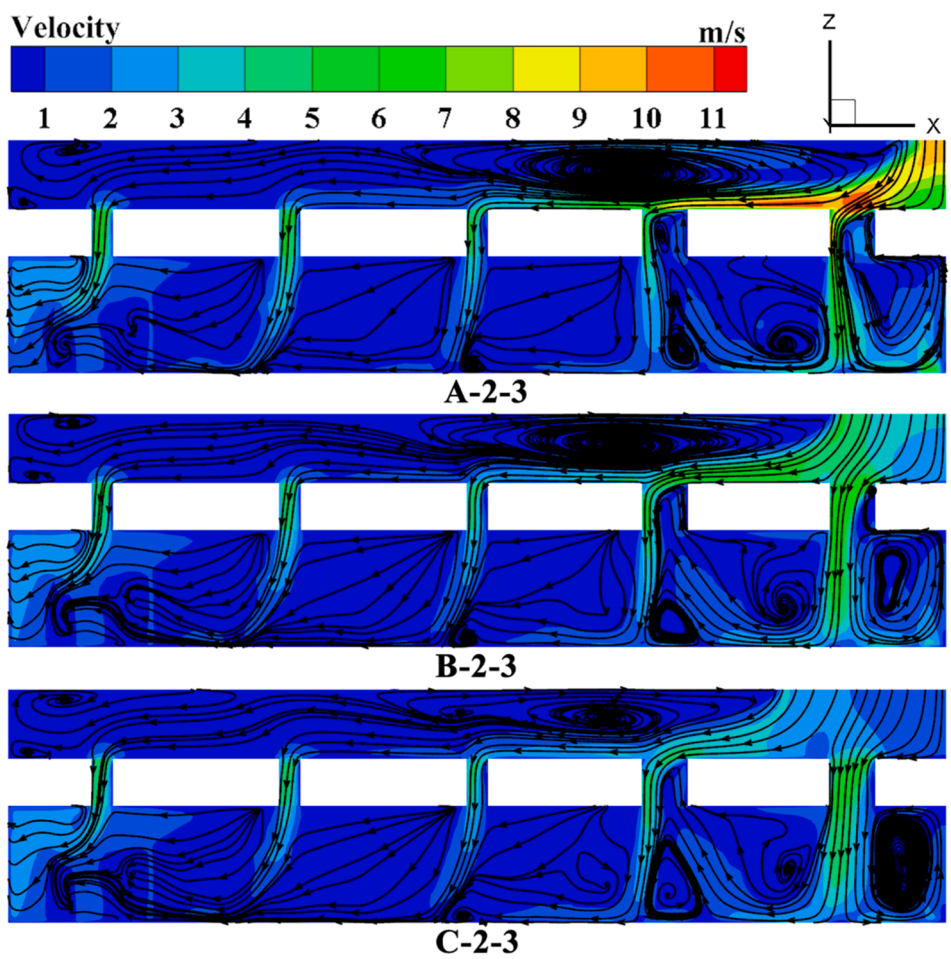

Fig. 19. Streamlines and contour of velocity magnitude for three different inlet diameters.

target plate, the maximum temperature decreases further for three kinds of jet orifice plates while the difference between the maximum temperature and the minimum temperature is basically unchanged due to the decrease of minimum temperature. For 1–1-NP, the temperature uniformity of the target surface is slightly enhanced compared with 1–1-UP while the temperature of the core region is still slighter higher than that of the edge region. However, as for 2–2-NP and 2–3-NP, the temperature uniformity of the target surface is essentially unvaried compared with 2–2-UP and 2–3-UP while the temperature in the core region is even lower than that of the edge region. In addition, it can be

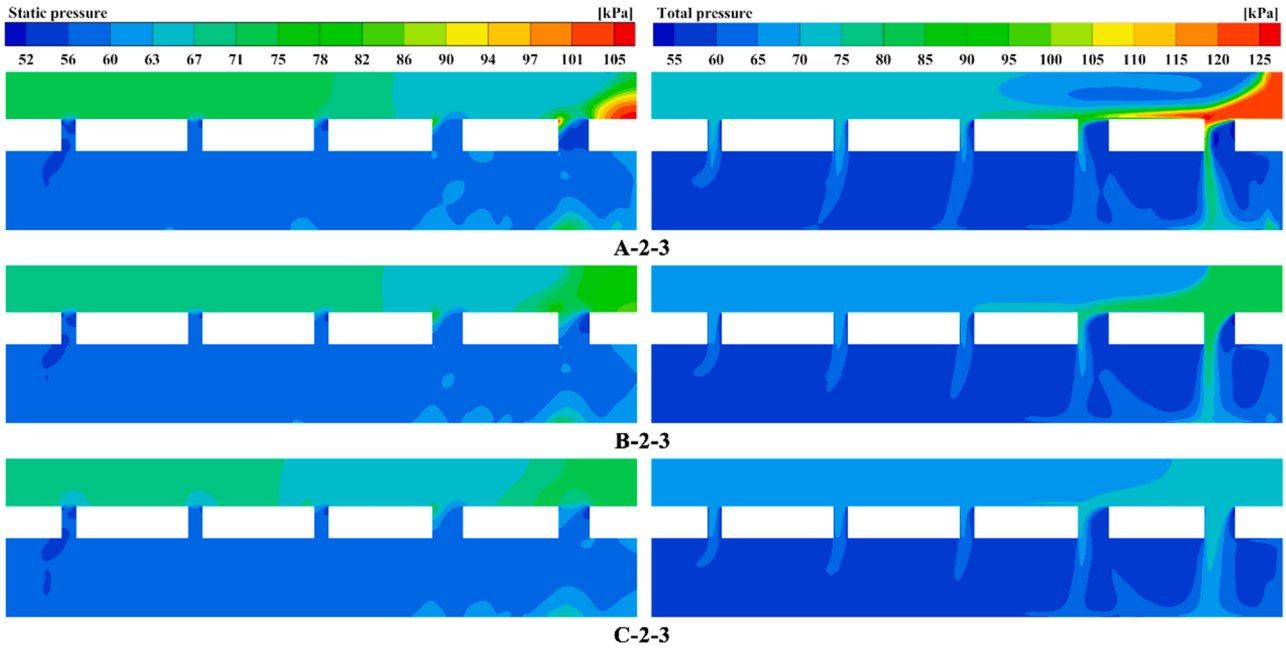

Fig. 20. Contour of static pressure and total pressure for three different inlet diameters.

found that the temperature is generally the lowest near the wall, which becomes more obvious after the introduction of the pin–fin arrays. This is agreed with the study by Wu et al. [51] that the influence from the adjacent wall enhances the heat transfer.

Fig. 13 displays the streamlines and contour of velocity magnitude of jet orifice plate 2–2 for three different target plates, i.e. smooth plate, uniform pin–fin plate and non-uniform pin–fin plate. Due to the influence of high horizontal velocity in the stagnation chamber, the flow in the jet No. 1–2 is relatively non-uniform compared with the jet No. 3–5. For smooth plate, resulting from the interaction between jet No. 1 and 2, a pair of large-scale vortices forms in the channel and deflects downstream slightly due to the crossflow. With the continuous enhancement of horizontal crossflow in the downstream, the number and scale of the vortices continue to shrink and eventually disappear at the jet No. 5. As for uniform and non-uniform pin–fin plates, due to the interaction between jet and pin-fins, many small-scale disordered vortex structures are produced between jet No. 1 and 2, especially evident in 2–2-NP. The breakdown of large vortex helps to generate strong turbulence, which is conductive to enhancing heat transfer [52]. In addition, different from the smooth plate, a small-scale vortex forms near the stagnation region of jet No. 3 and 4 for uniform and non-uniform pin–fin plates, respectively, and flow separation occurs beneath jet No. 5 resulting from the existence of pin-fins attenuating the effect of horizontal crossflow.

Fig. 14 presents the variation of surface average temperature and convective heat transfer coefficient with mass flow rate for three kinds of heat transfer plates within the mass flow rate range of 12.5–31.3 g/s. As shown in Fig. 14(a), the average temperature of the whole surface ($\overline{T}_w$) decrease with larger mass flow rate ($\dot{m}$) for all cases and the average temperature of smooth plate is significantly higher than that of uniform or non-uniform pin–fin plate with the maximum temperature difference about 20°C. However, the average heat transfer coefficient ($\overline{h}_t$) of the smooth plate is usually higher than that of uniform or non-uniform pin–fin plate under all the mass flow rate situations. The reason for the interesting phenomenon is that the total area of the heat transfer surface (base plus fins) is used to define the heat transfer coefficient and the area increasing effect caused by the introduction of pin–fin arrays will be neglected. The same phenomenon is also observed in our previous research [46] and the study by Trabold et al. [53] that in some conditions, the Nusselt number of smooth plate is higher than that of ribbed rough plate and the detailed analysis can be found in our previous study [46].

Fig. 14(c) shows the variation of average temperature of the core region ($\overline{T}_{w,core}$) with $\dot{m}$ for different heat transfer plates. Compared with Fig. 14(a), it is found that when the $\dot{m}$ is high, the $\overline{T}_{w,core}$ is even lower than the $\overline{T}_w$ for the non-uniform pin–fin plate with jet orifice plate 2–3. In addition, different from the smooth plate that jet orifice plate 2–2 achieves the lowest $\overline{T}_{w,core}$, the jet orifice plate 2–3 corresponds to the lowest $\overline{T}_{w,core}$ when the pin–fin arrays are introduced. Fig. 14(d) demonstrates the variation of average heat transfer coefficient of the core region ($\overline{h}_{t,core}$) with $\dot{m}$ for three different heat transfer plates. Similarly, the $\overline{h}_{t,core}$ of jet orifice plate 2–3 is significantly higher than that of jet orifice plate 2–2 when the pin–fin arrays are used, suggesting the increase of heat transfer area can take full advantage of the large flow rate in the core region.

3.2.2. Pressure drop characteristics

Fig. 15 presents the variation of total pressure drop with mass flow rate for three kinds of heat transfer plates. Generally, for all cases, the total pressure drop increases with larger mass flow rate. It is worth noting that changing the heat transfer plate type has little effect on the total pressure drop of the heat sink, especially when the mass flow rate is small. However, when the jet orifice plate is changed, there is a more significant influence on the total pressure drop. To further analyze the influence of different heat transfer plates, a detailed analysis is carried out when the mass flow rate is 25.08 g/s, as shown in Fig. 16. Visibly, when the jet orifice plate is the same, the heat sink with non-uniform pin–fin plate corresponds to the highest total pressure drop, followed by the uniform pin–fin plate and the smooth plate. However, the difference among the three heat transfer plates is relatively small and the

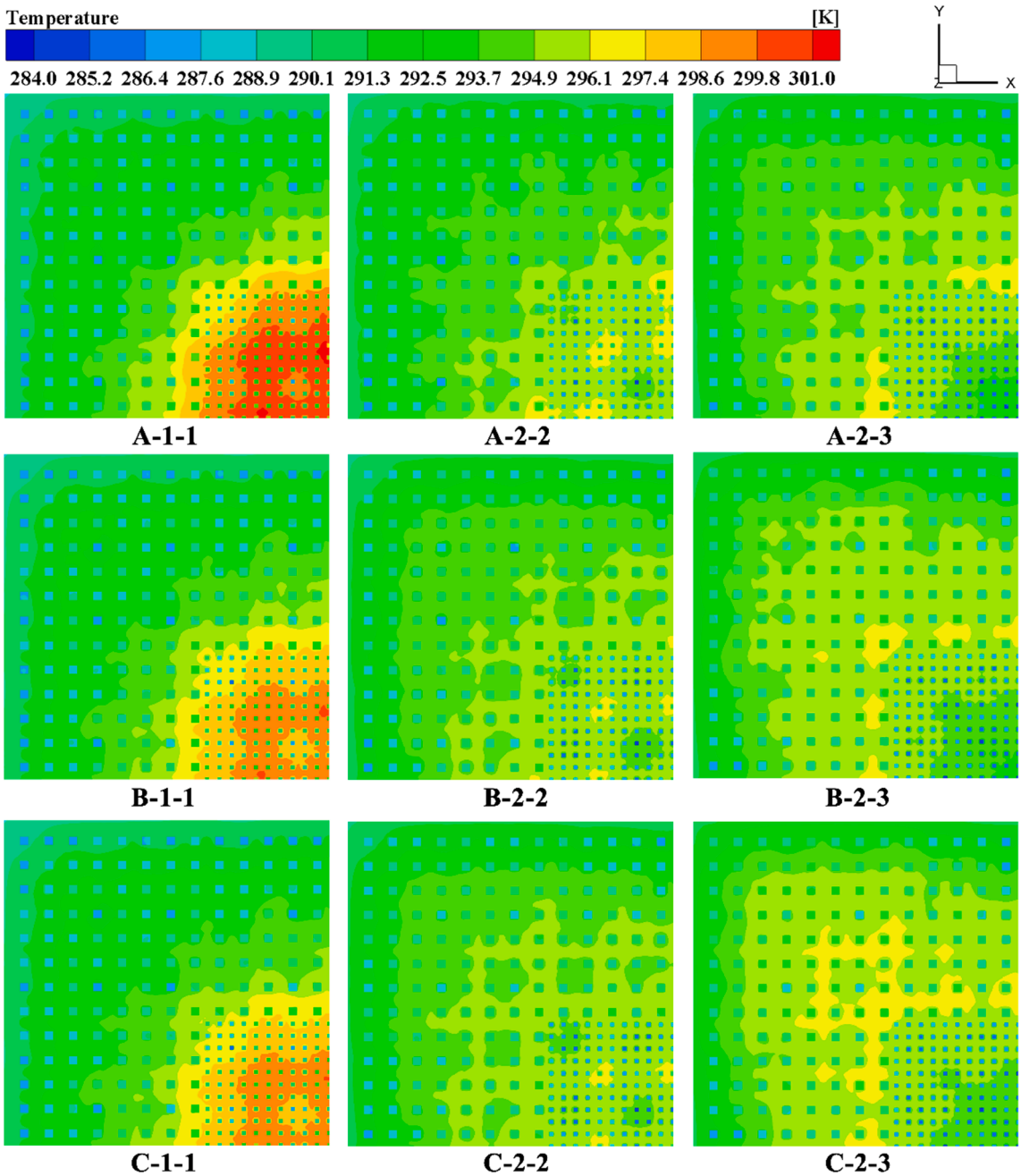

Fig. 21. The temperature contour map for three different inlet diameters ($q_h = 100$ W/cm^2,$q_l = 50$ W/cm^2,$\dot{m} = 25.08$ g/s).

total pressure drop of the non-uniform pin–fin plate is only about 3% higher than that of smooth plate. In addition, by analyzing the pressure drop composition, only ΔP_3 will change when the heat transfer plate type is changed, while ΔP_1 and ΔP_2 remain essentially the same, suggesting the introduction of pin–fin arrays will mainly change the flow field in heat transfer channel. However, changing the jet orifice plate type can have a significant effect on the pressure drop and cause obvious changes in the flow field in heat transfer channel and stagnation chamber.

3.3. Effect of inlet areas

According to above study, the total pressure drop of the heat sink is composed of three components, i.e. ΔP_1, ΔP_2 and ΔP_3, of which ΔP_1 accounts for the largest proportion. By adjusting the arrangement of jet holes, the pressure drop of heat sink is evidently reduced while achieving improved temperature uniformity of the heat transfer surface. However, the total pressure drop is still quite considerable, especially when the mass flow is large, and the total pressure drop exceeds 100 kPa. Hence, further optimizations of heat sink structure to improve the hydrodynamic performance are important and such improvements need

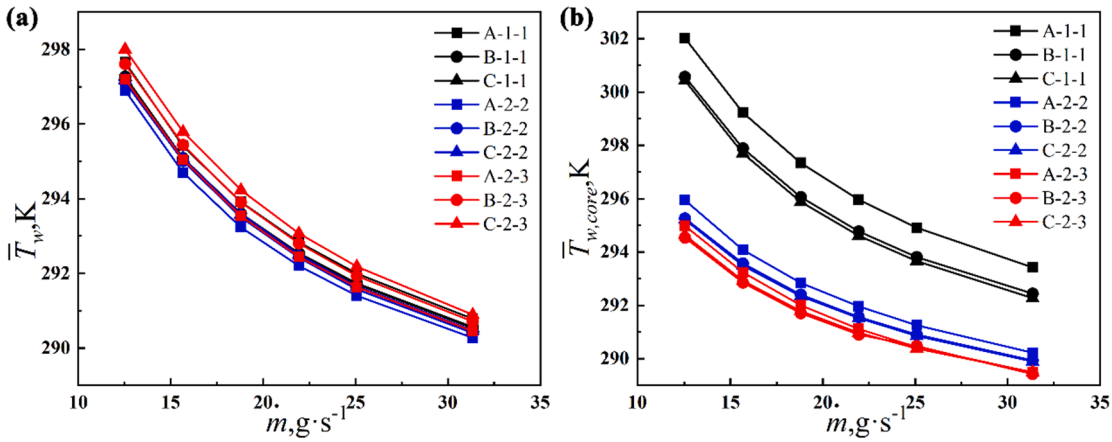

Fig. 22. The average temperature of the whole heat transfer surface (a) and the core region of the heat transfer surface (b) under different mass flow rates (q_h = 100 W/cm^2,q_l = 50 W/cm^2).

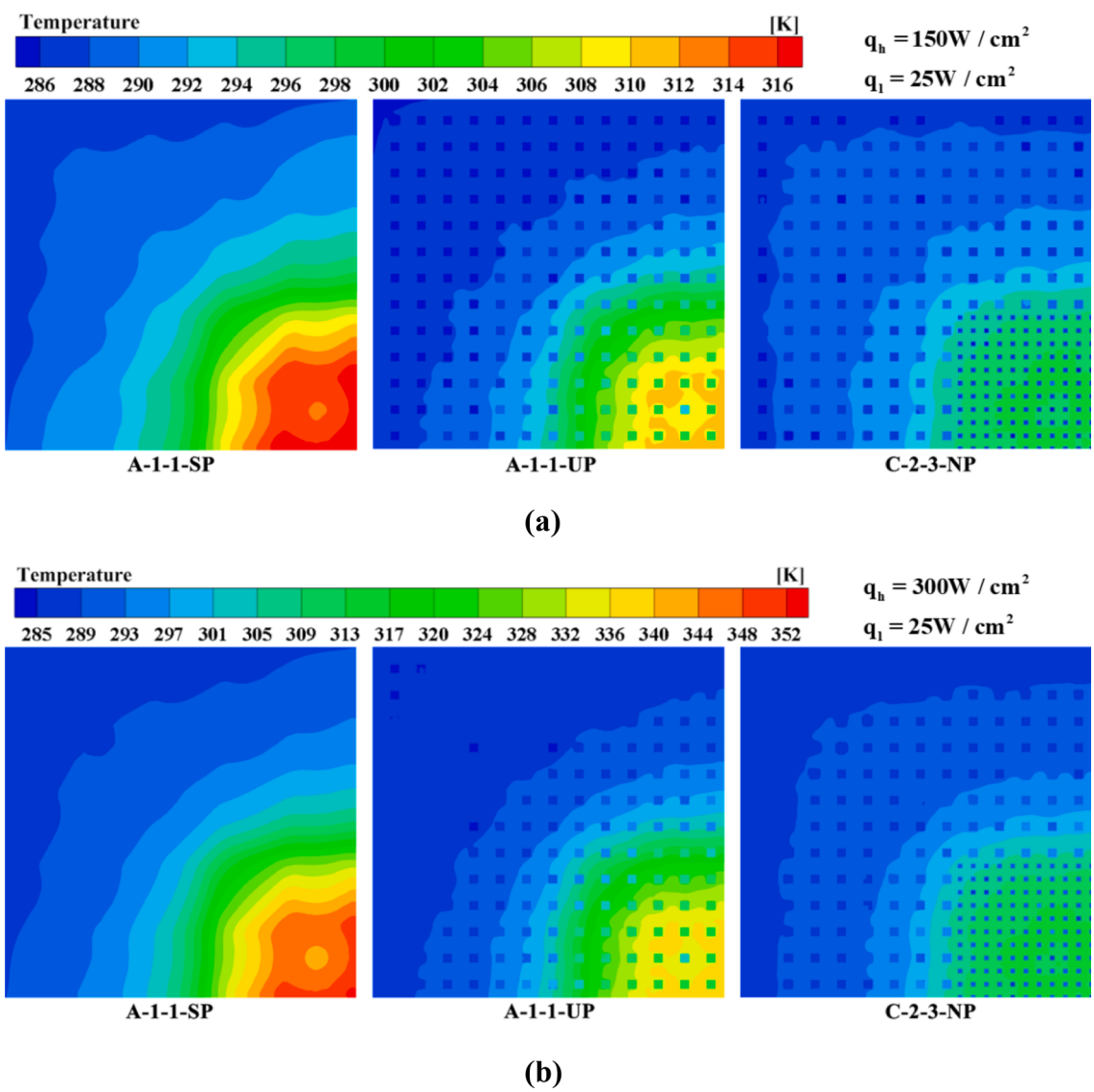

Fig. 23. Comparison of the well-designed heat sink against traditional heat sink for (a)q_h = 150 W/cm^2,q_l = 25 W/cm^2 and (b) q_h = 300 W/cm^2,q_l = 25 W/cm^2($\dot{m}$ = 31.3 g/s).

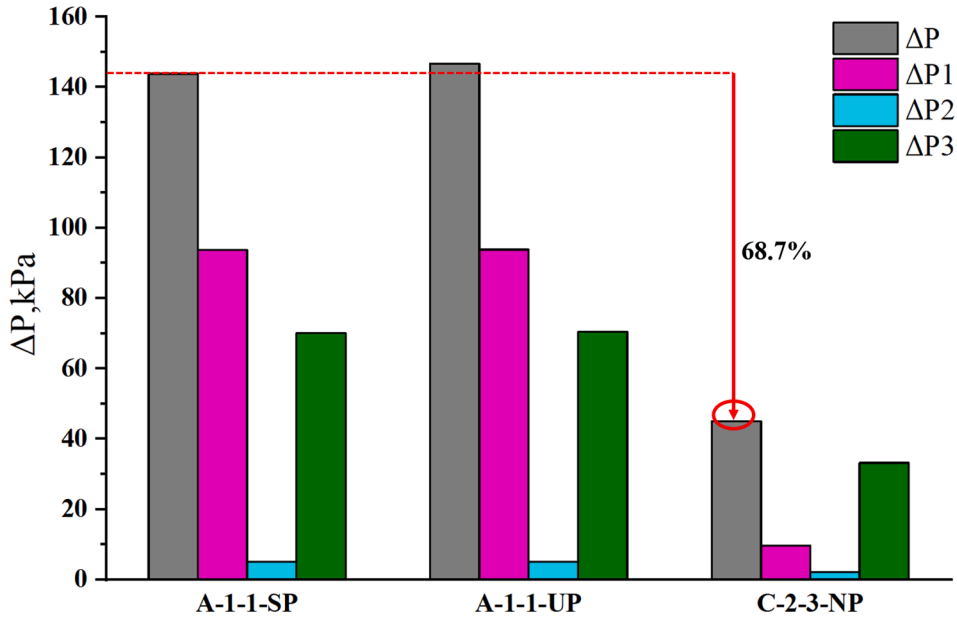

Fig. 24. Comparison of the pressure drop of the well-designed jet impingement heat sink and the conventional heat sink ($\dot{m}$ = 31.3 g/s).

Table 5
The detailed numerical values for well-designed and traditional heat sink [K].

Power maps		T_{max}	T_{min}	ΔT	$\overline{T}_w$	$\overline{T}_{w,core}$
q_h = 150 W/cm^2 q_l = 25 W/cm^2	A-1–1-SP	318.21	286.02	32.19	294.15	311.59
	A-1–1-UP	311.4	284.62	26.78	290.19	301.98
	C-2–3-NP	298.55	285.29	13.26	288.94	291.36
q_h = 300 W/cm^2 q_l = 25 W/cm^2	A-1–1-SP	352.39	286.14	66.25	300.79	337.85
	A-1–1-UP	339.21	284.76	54.45	294.66	319.69
	C-2–3-NP	313.73	285.78	27.95	291.93	299.03

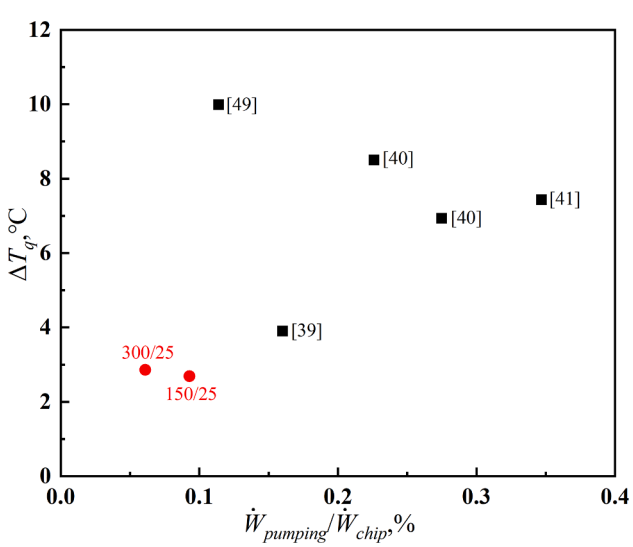

Fig. 25. Comparison of well-designed heat sink in this work (red colored text and symbols) against heat sinks from literature ($\dot{m}$ = 15.68 g/s). (For interpretation of the references to colour in this figure legend, the reader is referred to the web version of this article.)

Table 6
Comparison of the results of this paper against literature results.

Reference	q_h(W/cm^2)	q_l(W/cm^2)	$\dot{W}_{pumping}/\dot{W}_{chip}$(%)	ΔT_q(°C)
Xia et al.[54]	200	200	0.114	9.99
Brunschwiler et al. [45]	140[a]	40[a]	0.347	7.43
Danish et al.[43]	300	50	0.16	3.9
Lee et al.[44]	400	85	0.275	6.93
	300	85	0.226	8.5
Current work	150	25	0.093	2.69
	300	25	0.061	2.86

[a] Approximate values back calculated from available information.

to be easy to implement in practical engineering applications. From the previous analysis we know that the impact loss and resistance loss along the inlet chamber are the main source of ΔP_1, so we propose the possibility of slowing the velocity at the inlet by increasing the inlet area, which does not lead to large structural changes and is easy to implement in practical applications. Fig. 1(Ⅳ) displays the three different diameters of the heat sink inlet, type A, B, and C, respectively, where type A has been used in the above study. In addition, the 1–1, 2–2 and 2–3 jet orifice plates and the non-uniform pin–fin plate are selected to study the effect of inlet area.

Fig. 17 depicts the variation of total pressure drop with mass flow rate for three different inlet diameters. Apparently, the pressure drop will be dramatically reduced when using the larger inlet diameter, especially at high flow rates. Additionally, the jet orifice plate 2–3 corresponds to the lowest pressure drop when using the largest inlet diameter, and the pressure drop is only about 6 kPa and 45 kPa at minimum and maximum flow rates respectively. To further investigate the specific variations of different components of the total pressure drop, a detailed analysis is carried out when the mass flow rate is 25.08 g/s, as illustrated in Fig. 18. Specifically, the reduction in total pressure drop is mainly attributed to the decrease in ΔP_1, which is in line with the expectations. In addition, the larger the jet hole area in the core region, the more obvious the effect of changing the inlet diameter on the total pressure drop. As marked in Fig. 18, when the jet orifice plate is 1–1, the total pressure drop is reduced by 26.6% by changing the inlet area, while 42.6% decrease is achieved by using jet orifice plate 2–3. Fig. 19 represents the streamlines and contour of velocity magnitude for different

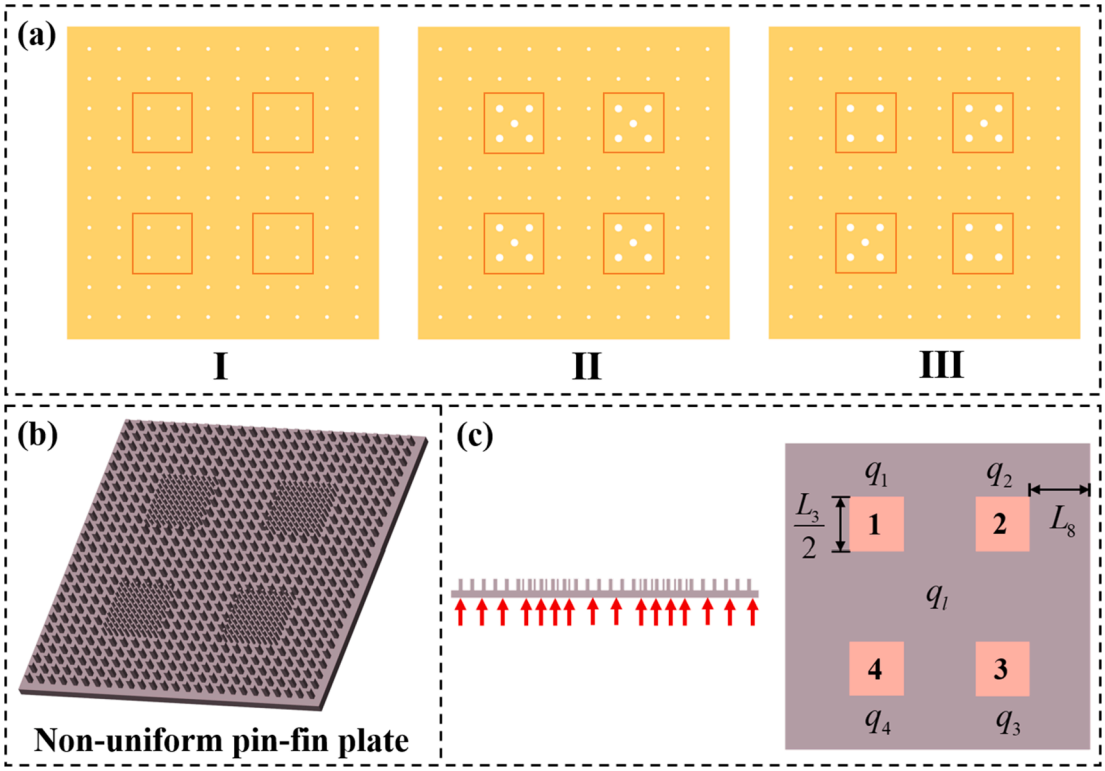

Fig. 26. The 3D model diagram of jet orifice plate, heat transfer plate and heat flux distribution in (a), (b) and (c).

inlet diameters with jet orifice plate 2–3, and the contour of static pressure and total pressure can be found in Fig. 20. Obviously, when the mass flow rate is the same, the increase of the inlet area will greatly reduce the inlet velocity, so the impact loss will be reduced. In addition, the velocity of horizontal crossflow formed by inlet fluid impacting the jet orifice plate decreases with larger inlet diameter, thus the fluid will be more likely to flow out of the jet hole near the core region, leading to a lower along-path loss in the inlet chamber. When the C type inlet is used, compared with jet orifice plate 1–1, more fluid will flow from the jet hole in the core region for jet orifice plate 2–3, which further reduces the horizontal crossflow velocity in the inlet chamber and the along-path loss also greatly reduces. As a result, the pressure drop of jet orifice plate 2–3 varies more obviously by changing the inlet diameter.

Additionally, for three different jet orifice plates, i.e. 1–1, 2–2 and 2–3, as the inlet area increases, ΔP_3 climbs up first then decline slightly. The main reasons we speculate are as follows. Firstly, the sudden increase of inlet area leads to more fluid flows out of the jet hole in the core region, thus more fluid needs to take a longer path to get out of the heat sink in the heat transfer channel, which results in greater along-path loss. Therefore, a sudden rise in ΔP_3 can be seen. However, as the inlet area increases further, the jet flow in the core region becomes more uniform, which leads to a lower velocity of jet flow, as shown in Fig. 20. As a result, the impact loss in the heat transfer channel will be declined, which is reflected in a slight drop in ΔP_3.

Fig. 21 displays the temperature contour map for three different inlet diameters at the mass flow rate of 25.08 g/s. Unlike the dramatic change in pressure drop, changing the inlet diameter has less effect on the heat transfer performance. When the jet orifice plate is 2–2 and 2–3, the temperature distribution in the core region is almost unchanged for three different inlet diameters. As for jet orifice plate 1–1, the temperature in the core region will decreases evidently when the inlet type changing from A to B, while the temperature distribution mostly maintains the same as the inlet type changing from B to C, which can also be corroborated in Fig. 22(b). Fig. 22(a) represents the variation of average temperature of the whole heat transfer surface with different mass flow rate. Similar to the previous situation, changing the inlet diameter has less effect on the overall heat transfer performance. However, as shown in Fig. 22(b), changing the inlet diameter has the greatest influence on $\overline{T}_{w,core}$ of heat sink with jet orifice plate 1–1.

3.4. Extension to higher heat flux and comparison with the literature

According to above numerical simulation, it is found that the temperature uniformity of the heat transfer surface and the resistance performance are significantly improved when the hotspot-targeted jet orifice plate and heat transfer plate are used. The heat sink with jet orifice plate 2–3, non-uniform pin–fin plate and largest inlet diameter achieves the best thermal–hydraulic performance and is selected as the well-designed structure. To further explore the performance of hotspot-targeted jet impingement heat sink under more severe conditions, we calculated the results for another two heat flux maps, i.e. $q_h = 150\text{W/cm}^2, q_l = 25\text{W/cm}^2$ and $q_h = 300\text{W/cm}^2, q_l = 25\text{W/cm}^2$, and compared with the traditional heat sink designs. Figs. 23 and 24 represent the comparison of temperature contour map and pressure drop histogram, respectively. More specifically, the well-designed heat sink achieves an improvement of 58% in ΔT while the pressure drop is reduced by 68.7% as compared to the traditional design (see Table 5 and Fig. 25).

In addition, the hotspot-targeted jet impingement heat sink is also compared against the microchannel heat sinks in the literature, designed to reduce ΔT. Since the literature results for ΔT have been calculated under different conditions of heat flux distribution, we normalized ΔT for comparison by drawing on the equation proposed by Chander et al. [42]. Eq. (12) implies that a design is better if it achieves lower ΔT with

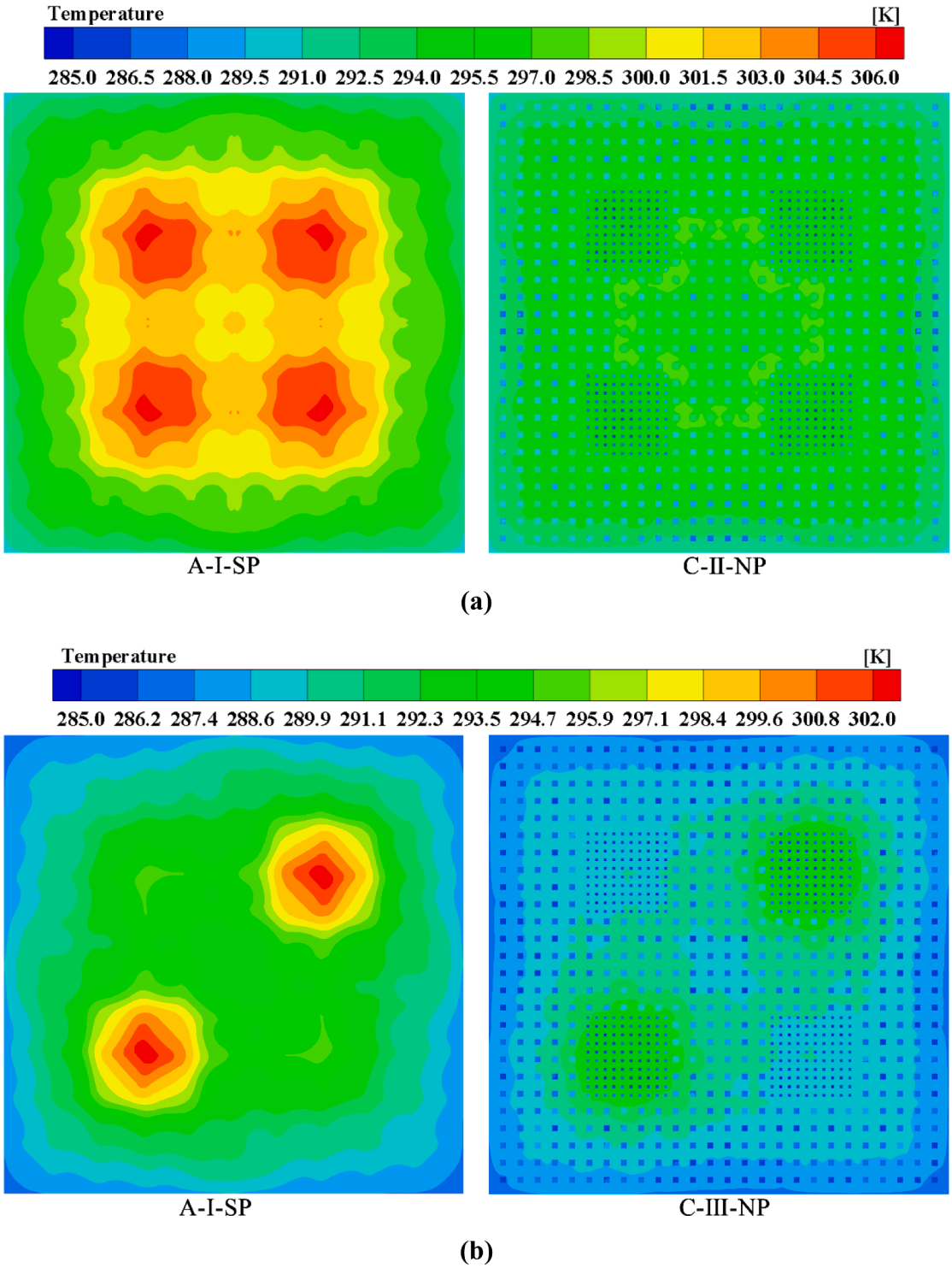

Fig. 27. Comparison of the temperature contour map under different heat flux distribution for (a) $q_l = 50$ W/cm^2, $q_1 = q_2 = q_3 = q_4 = 100$ W/cm^2 and (b) $q_l = 25$ W/cm^2,$q_1 = q_3 = 50$ W/cm^2,$q_2 = q_4 = 100$ W/cm^2($\dot{m} = 100.3$ g/s).

higher q_h/q_l.

$$\Delta T_q = \frac{\Delta T}{\left(\frac{q_h}{q_l}\right)} \tag{12}$$

Fig. 25 displays the comparison of well-designed heat sink in this work against the heat sinks from literature, and the detailed information are illustrated in Table 6. Notably, the well-designed heat sink achieves ΔT_q values of 2.69 and 2.86 while the pump power consumption accounts for only 0.093% and 0.061%, which indicates the design in this work compares favorably against the literature designs. In addition, the ΔT_q will continue to decline lightly with larger mass flow rate, but the pump power consumption will increase significantly. Compared with the optimization strategy adopted in the microchannel heat sink [43], the combination of optimized jet hole and pin–fin arrays can significantly enhance the heat transfer performance in the core region by using

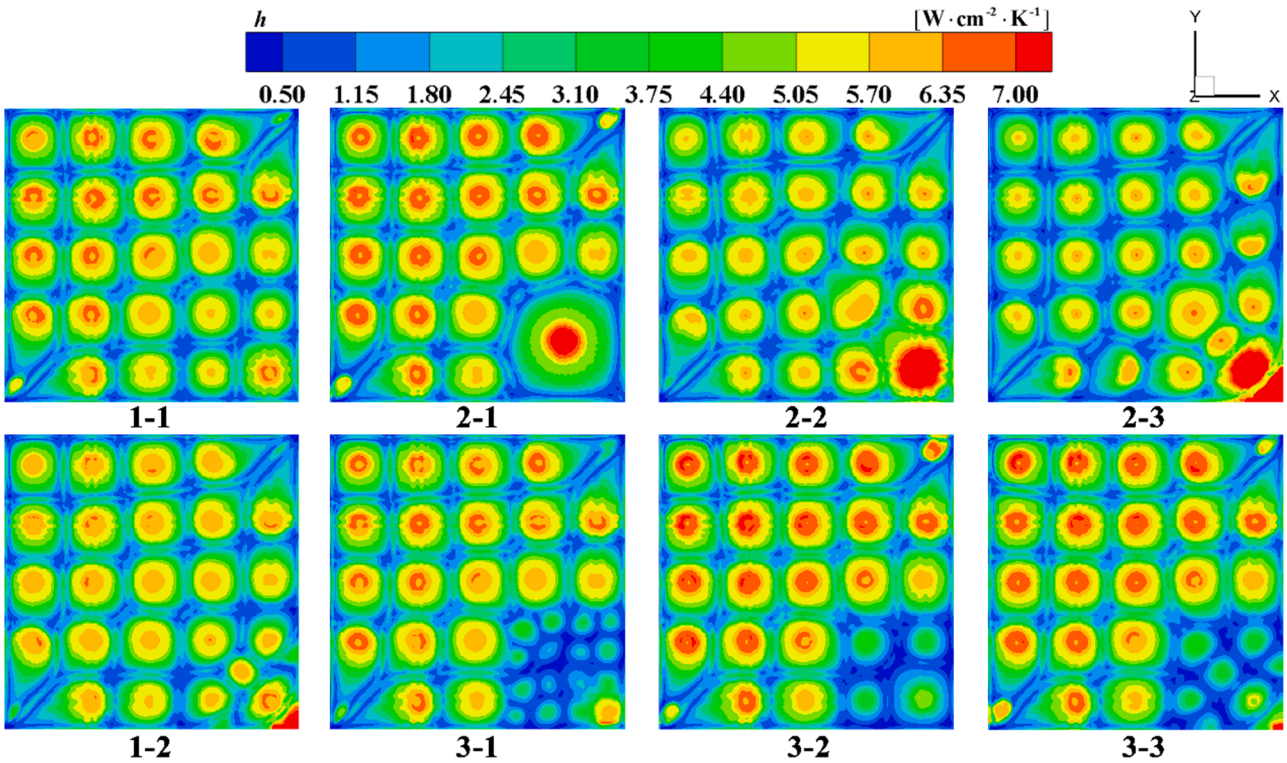

Fig. 28. The local heat transfer coefficient contour map of smooth plate with different jet orifice plates (D_{in} = 4mmq_h = 100 W/cm^2,q_l = 50 W/cm^2,$\dot{m}$ = 25.08 g/s).

the area increasing effect and direct fluid scouring effect.

4. Design strategies for hotspot-targeted jet impingement heat sink

By analyzing the numerical results of heat sink with different structures, we recommend some design strategies that can be referend to in the design of hotspot-targeted jet impingement heat sink. The design strategies consist of:

(1) Appropriately increasing the number and diameter of jet hole in the core region can effectively adjust the jet flow distribution, so that more fluid washes against the core region and improves the temperature uniformity. However, too many jet hole numbers or too large jet hole diameter may lead to heat transfer deterioration in the core region, which needs to be properly optimized according to the actual application.
(2) By introducing pin–fin arrays on the heat transfer surface, the heat transfer performance can be greatly enhanced due to the increase of heat transfer area and better flow mixing. In addition, the use of small-sized pin fins in the core region can further improve the heat transfer performance without causing a large increase in pressure drop.
(3) The inlet area of the heat sink has a significant impact on the total pressure drop. On the premise of meeting the requirement of actual use, increasing the inlet area can dramatically reduce the impact loss and along-path loss at the inlet stagnation chamber, especially for large flow conditions.

5. Conclusion

A novel jet impingement cooling concept, for hotspot-targeted, energy efficient cooling of non-uniform heat generation electronics, was proposed in this work. A single-phase three-dimensional conjugate heat transfer analysis based on the Naiver-Stokes equations was used to investigate the thermal hydraulic performance of the hybrid micro pin–fin, jet impingement heat sink. Based on the simulation results, the following conclusions are drawn:

(1) Under the same inlet mass flow rate and the same arrangement of jet holes, the smaller the diameter in the core area is, the less fluid passes through the jet hole to wash against the heat transfer surface. By appropriately increasing the number and diameter of jet hole in the core region, the jet flow distribution will be effectively adjusted, and the heat transfer performance of the core region will be greatly enhanced.
(2) Compared with smooth plate and uniform pin–fin plate, the maximum temperature rise of non-uniform pin–fin plate is the lowest, and the heat transfer performance in the core region is the best, owing to the increase of heat transfer area and better flow mixing. However, compared with changing the type of jet orifice plate, the introduction of pin–fin arrays has little effect on the total pressure drop of the heat sink. Generally, when the jet orifice plate is the same, the heat sink with non-uniform pin–fin plate corresponds to the highest total pressure drop, followed by the uniform pin–fin plate and the smooth plate.
(3) When the mass flow rate is the same, the increase of the inlet area will greatly reduce the inlet velocity, thus the impact loss and the along-path loss in the inlet chamber will be dramatically reduced. In addition, the larger the jet hole area in the core region, the more obvious the effect of changing the inlet diameter on the total pressure drop. However, unlike the dramatic change in pressure drop, changing the inlet diameter has less effect on the heat transfer performance. As a result, the large inlet diameter of

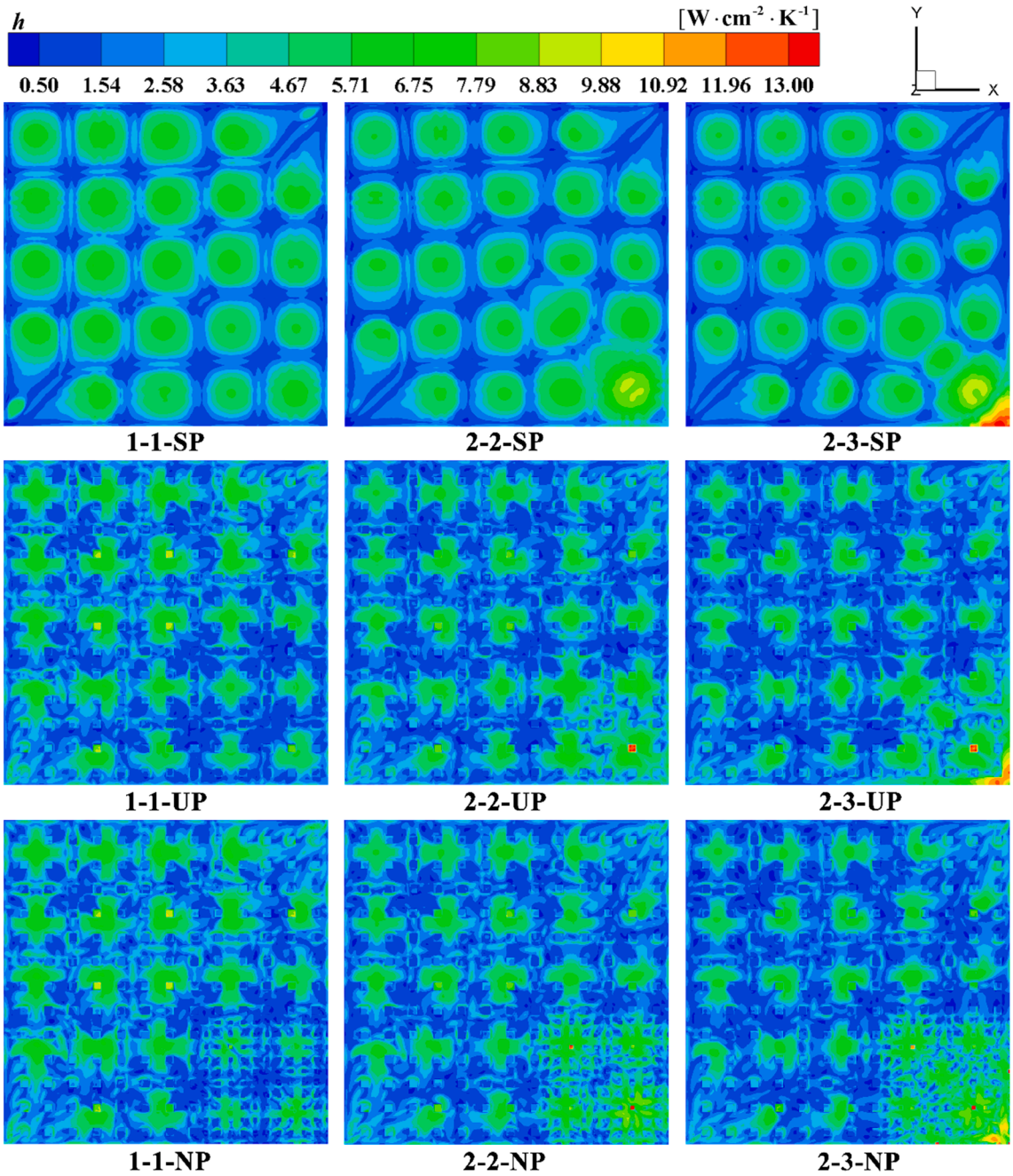

Fig. 29. The local heat transfer coefficient contour map of three different impingement surface types (D_{in} = 4mm,q_h = 100 W/cm^2,q_l = 50 W/cm^2,$\dot{m}$ = 25.08 g/s).

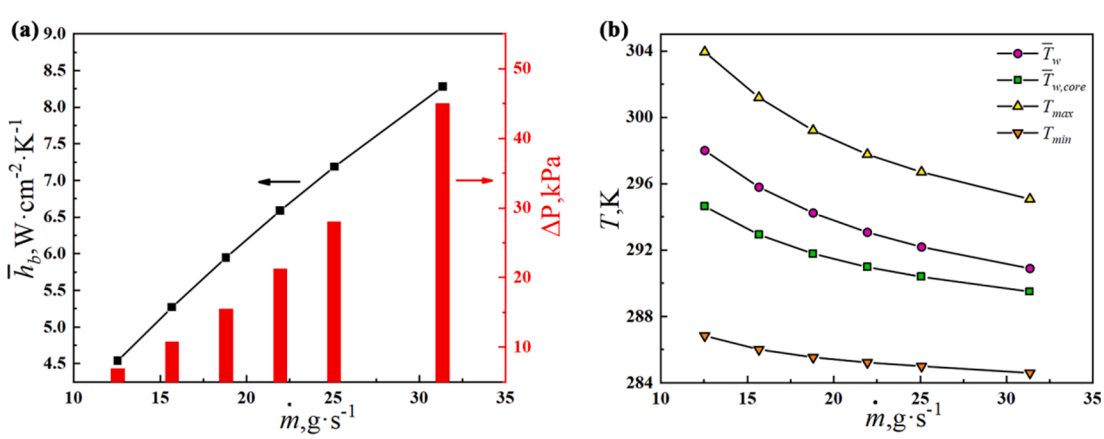

Fig. 30. The overall thermal–hydraulic performance of the well-designed structure under different mass flow rates (q_h = 100 W/cm^2,q_l = 50 W/cm^2).

heat sink should be used under the premise of design requirement, especially for high flow conditions.

(4) The heat sink with jet orifice plate 2–3, non-uniform pin–fin plate and largest inlet diameter achieves the best thermal hydraulic performance and is selected as the well-designed structure. Compared with the traditional jet impingement heat sink, the optimal design achieves an improvement of 58% in temperature non-uniformity while the total pressure drop is reduced by 68.7% at the same mass flow rate. In addition, the pumping power consumption for optimal design is only 0.093% and 0.061% of the total heating power for 150 W/cm^2 and 300 W/cm^2 hotspot heat flux respectively while ensuring the acceptable temperature non-uniformity, which compares favorably against the literature designs.

Declaration of Competing Interest

The authors declare that they have no known competing financial interests or personal relationships that could have appeared to influence the work reported in this paper.

Acknowledgement

This work was supported by the National Natural Science Foundation of China (grant no. 51736004).

Appendix

1. The governing equation and convergence conditions used in the simulation

In the simulation, the fluid flow and heat transfer can be described by the continuity equation, momentum equation and energy equation.

Continuity equation:

$$\frac{\partial(\rho u_i)}{\partial x_i} = 0 \tag{13}$$

Momentum conservation equation:

$$\frac{\partial(\rho u_i u_j)}{\partial x_j} = -\frac{\partial p}{\partial x_i} + \frac{\partial}{\partial x_j}\left(\mu\frac{\partial u_i}{\partial x_j} - \rho\overline{u_i' u_j'}\right) \tag{14}$$

Energy conservation equation:

$$\frac{\partial(u_i T)}{\partial x_j} = \frac{\partial}{\partial \mathrm{x_j}}\left(\frac{\lambda_{eff}}{\rho c_p}\frac{\partial \mathrm{T}}{\partial \mathrm{x_j}}\right) \tag{15}$$

Kinetic energy equation:

$$\frac{\partial}{\partial x_i}(\rho k u_i) = \frac{\partial}{\partial \mathrm{x_j}}\left[\left(\eta + \frac{\eta_t}{\sigma_k}\right)\frac{\partial \mathrm{k}}{\partial \mathrm{x_j}}\right] + 2\eta_t\frac{\partial \mathrm{u_i}}{\partial \mathrm{x_j}}S_{i,j} - \rho\varepsilon \tag{16}$$

Dissipation rate equation:

$$\frac{\partial}{\partial x_i}(\rho k u_i) = \frac{\partial}{\partial \mathrm{x_i}}\left[\left(\eta + \frac{\eta_t}{\sigma_\varepsilon}\right)\frac{\partial \varepsilon}{\partial \mathrm{x_i}}\right] + 2C_{1\varepsilon}\frac{\varepsilon}{k}\eta_t\frac{\partial \mathrm{u_i}}{\partial \mathrm{x_j}}S_{i,j} - C_{2\varepsilon}\rho\frac{\varepsilon^2}{k} \tag{17}$$

The energy equation in the solid domain:

$$\frac{\partial}{\partial x_i}\left(k_s\frac{\partial T}{\partial x_i}\right) = 0 \tag{18}$$

In the above formula, ρ is the liquid density, p is the pressure, u_i is the speeds in the $\times$, y, and z directions, c_p is the constant pressure specific heat capacity, η_t is the eddy viscosity coefficient and k_s is the thermal conductivity of the solid. $S_{i,j}$, η_t and $C_{1\varepsilon}$ are given by the following equation, where $C_{2\varepsilon}$ is 1.68 and C_μ is 0.085.

$$\eta_t = \rho C_\mu\frac{k}{\varepsilon} \tag{19}$$

$$S_{i,j} = \frac{1}{2}\left(\frac{\partial \mathrm{u_i}}{\partial \mathrm{x_j}} + \frac{\partial \mathrm{u_j}}{\partial \mathrm{x_i}}\right) \tag{20}$$

$$C_{1\varepsilon} = 1.42 - \frac{\overline{\eta}(1-\overline{\eta}/4.38)}{1+0.015\overline{\eta}^3} \tag{21}$$

The SIMPLE algorithm is adopted for pressure–velocity coupling, and the discretization scheme is set as the standard for the pressure, QUICK for energy, and second-order upwind for the remaining period. When the residuals of continuum equation and momentum equation reach 10^{-5}, the convergence residuals of turbulence dissipation term reach 10^{-4}, and the convergence residuals of energy equation are less than 10^{-7}, then the numerical calculation is considered to be convergent.

2. The verification of multi-core hotspot heat dissipation

In order to verify the effectiveness of design strategy obtained in the cases with a single hotspot, we conduct the overall numerical simulation for the case with four hotspots. Fig. 26(c) depicts the distribution of four hotspots at the bottom of the heat transfer plate, and Fig. 26(a) and Fig. 26 (b) respectively show the three kinds of jet orifice plates and the non-uniform pin–fin plate designed according to the hotspots distribution. Jet orifice plate I presents the traditional jet hole arrangement while jet orifice plate II and III present the optimized jet hole arrangement. In addition, the dimensions of the jet orifice plate and heat transfer plate are the same as those in Fig. 1, and the same meshing strategy are adopted.

Fig. 27(a) displays the temperature contour map of heat transfer surface assuming that the heat flux of the four hotspots is uniform. As with the

single hotspot situation, the optimal heat sink C-II-NP has a more uniform temperature distribution, and the maximum temperature of C-II-NP is nearly 10°C lower than that of A-I-SP. Additionally, in practical situation, the heat production of each hotspot may not be the same, so we also investigate the situation with non-uniform heat production of hotspots, and adjust the arrangement of jet holes according to the heat flux distribution. For C-III-NP shown in Fig. 27(b), the average temperature of hot spot 2 and 4 is only 2 °C higher than that of hot spot 1 and 3 under the heat flux difference of 50 W/cm^2. However, as for A-I-SP, the temperature difference is three times that of C-III-NP. From the above numerical simulation results, it can be found that the design strategies concluded in the single core hotspot heat dissipation are still effective in the case with multi-core hotspot. Nevertheless, compared with the actual chip heat dissipation, the study in this paper is simplified, so the design strategies for hotspot-targeted jet impingement heat sink should be appropriately adjusted according to the practical situation.

3. Supplement materials

See Figs. 28–30.

References

[1] L. Wang, L.L. Wang, D.J. Shang, C. Zhuo, P.Q. Zhou, Ieee, Optimizing the Energy Efficiency of Power Supply in Heterogeneous Multicore Chips with Integrated Switched-Capacitor Converters, in: 2019 Design, Automation & Test in Europe Conference & Exhibition, IEEE, New York, 2019, pp. 836–841.

[2] M.S. Shamim, R.S. Narde, J.L. Gonzalez-Hernandez, A. Ganguly, J. Venkatarman, S.G. Kandlikar, Evaluation of wireless network-on-chip architectures with microchannel-based cooling in 3D multicore chips, Sustain. Comput.-Inform. Syst. 21 (2019) 165–178.

[3] C. Nadjahi, H. Louahlia, S. Lemasson, A review of thermal management and innovative cooling strategies for data center, Sustain. Comput.-Inform. Syst. 19 (2018) 14–28.

[4] S.M.S. Murshed, C.A.N. de Castro, A critical review of traditional and emerging techniques and fluids for electronics cooling, Renew. Sustain. Energy Rev. 78 (2017) 821–833.

[5] X.B. Luo, R. Hu, S. Liu, K. Wang, Heat and fluid flow in high-power LED packaging and applications, Prog. Energy Combust. Sci. 56 (2016) 1–32.

[6] I. Mudawar, Assessment of high-heat-flux thermal management schemes, IEEE Trans. Compon. Packag. Technol. 24 (2001) 122–141.

[7] S.N. Li, H.N. Zhang, J.P. Cheng, X.B. Li, W.H. Cai, Z.Y. Li, F.C. Li, A state-of-the-art overview on the developing trend of heat transfer enhancement by single-phase flow at micro scale, Int. J. Heat Mass Transf. 143 (2019) 118476.

[8] Z.G. Li, Y. Haramura, D.W. Tang, C.H. Guo, Analysis on the heat transfer characteristics of a micro-channel type porous-sheets Stirling regenerator, Int. J. Therm. Sci. 94 (2015) 37–49.

[9] F. Pourfattah, A.A.A. Arani, M.R. Babaie, H.M. Nguyen, A. Asadi, On the thermal characteristics of a manifold microchannel heat sink subjected to nanofluid using two-phase flow simulation, Int. J. Heat Mass Transf. 143 (2019) 118518.

[10] Z. Yan, X. Huang, C. Yang, Hydrodynamic effects on particle deposition in microchannel flows at elevated temperatures, J. Heat Transf.-Trans. ASME 140 (2018), 012402.012401–012402.012410.

[11] D.B. Tuckerman, R.F.W. Pease, High-performance heat sinking for VLSI, IEEE Electron. Device Lett. 2 (1981) 126–129.

[12] G.D. Xia, D.D. Ma, Y.L. Zhai, Y.F. Li, R. Liu, M. Du, Experimental and numerical study of fluid flow and heat transfer characteristics in microchannel heat sink with complex structure, Energy Convers. Manage. 105 (2015) 848–857.

[13] D.X. Deng, W. Wan, Y. Tang, Z.P. Wan, D.J. Liang, Experimental investigations on flow boiling performance of reentrant and rectangular microchannels - a comparative study, Int. J. Heat Mass Transf. 82 (2015) 435–446.

[14] L. Chai, G. Xia, L. Wang, M. Zhou, Z. Cui, Heat transfer enhancement in microchannel heat sinks with periodic expansion–constriction cross-sections, Int. J. Heat Mass Transf. 62 (2013) 741–751.

[15] A. Rajalingam, S. Chakraborty, Effect of micro-structures in a microchannel heat sink - a comprehensive study, Int. J. Heat Mass Transf. 154 (2020) 119617.

[16] Y.L. Zhai, Z.H. Li, H. Wang, J.X. Xu, Thermodynamic analysis of the effect of channel geometry on heat transfer in double-layered microchannel heat sinks, Energy Convers. Manage. 143 (2017) 431–439.

[17] M.K. Sung, I. Mudawar, Effects of jet pattern on single-phase cooling performance of hybrid micro-channel/micro-circular-jet-impingement thermal management scheme, Int. J. Heat Mass Transf. 51 (2008) 4614–4627.

[18] M.A. Ebadian, C.X. Lin, A review of high-heat-flux heat removal technologies, J. Heat Transf.-Trans. ASME 133 (2011) 110801.

[19] W. Liu, P. Liu, Z.M. Dong, K. Yang, Z.C. Liu, A study on the multi-field synergy principle of convective heat and mass transfer enhancement, Int. J. Heat Mass Transf. 134 (2019) 722–734.

[20] F.L. Cui, F.J. Hong, P. Cheng, Comparison of normal and distributed jet array impingement boiling of HFE-7000 on smooth and pin-fin surfaces, Int. J. Heat Mass Transf. 126 (2018) 1287–1298.

[21] F.J. Hong, C.Y. Zhang, W. He, P. Cheng, G. Chen, Confined jet array impingement boiling of subcooled aqueous ethylene glycol solution, Int. Commun. Heat Mass Transf. 56 (2014) 165–173.

[22] R.S. Snedeker, A study of free jet impingement. Part 1. Mean properties of free and impinging jets, J. Fluid Mech. 45 (1971) 281–319.

[23] C.D. Donaldson, R.S. Snedeker, D.P. Margolis, A study of free jet impingement. Part 2. Free jet turbulent structure and impingement heat transfer, J. Fluid Mech. 45 (1971) 477–512.

[24] L. Jiji, Z. Dagan, Experimental investigation of single-phase multijet impingement cooling of an array of microelectronic heat sources, Cool. Technol. Electron. Equip. (1988) 333–351.

[25] M.M. Sorour, W.M. El-Maghlanr, M.A. Alnakeeb, A.M. Abbass, Experimental study of free single jet impingement utilizing high concentration SiO2 nanoparticles water base nanofluid, Appl. Therm. Eng. 160 (2019) 10.

[26] A.J. Robinson, E. Schnitzler, An experimental investigation of free and submerged miniature liquid jet array impingement heat transfer, Exp. Therm. Fluid Sci. 32 (2007) 1–13.

[27] D.J. Womac, S. Ramadhyani, F.P. Incropera, Correlating equations for impingement cooling of small heat sources with single circular liquid jets, J. Heat Transf. 115 (1993) 106–115.

[28] A.M. Kiper, Impinging water jet cooling of VLSI circuits, Int. Commun. Heat Mass Transf. 11 (1984) 517–526.

[29] M. Fabbri, V.K. Dhir, Optimized heat transfer for high power electronic cooling using arrays of microjets, J. Heat Transf.-Trans. ASME 127 (2005) 760–769.

[30] E.N. Wang, L. Zhang, L.N. Jiang, J.M. Koo, J.G. Maveety, E.A. Sanchez, K. E. Goodson, T.W. Kenny, Micromachined jets for liquid impingement cooling of VLSI chips, J. Microelectromech. Syst. 13 (2004), 1072-1072.

[31] T.W. Wei, H. Oprins, V. Cherman, G. Van der Plas, I. De Wolf, E. Beyne, M. Baelmans, Experimental characterization and model validation of liquid jet impingement cooling using a high spatial resolution and programmable thermal test chip, Appl. Therm. Eng. 152 (2019) 308–318.

[32] S. Ndao, Y. Peles, M.K. Jensen, Multi-objective thermal design optimization and comparative analysis of electronics cooling technologies, Int. J. Heat Mass Transf. 52 (2009) 4317–4326.

[33] S. Ndao, H.J. Lee, Y. Peles, M.K. Jensen, Heat transfer enhancement from micro pin fins subjected to an impinging jet, Int. J. Heat Mass Transf. 55 (2012) 413–421.

[34] P. Sullivan, S. Ramadhyani, F. Incropera, Use of smooth and roughened spreader plates to enhance impingement cooling of small heat sources with single circular liquid jets, Topics Heat Transf. HTD 206–2 (1993) 103–110.

[35] A. Husain, M. Ariz, N.Z.H. Al-Rawahi, M.Z. Ansari, Thermal performance analysis of a hybrid micro-channel, -pillar and -jet impingement heat sink, Appl. Therm. Eng. 102 (2016) 989–1000.

[36] X.M. Huang, W. Yang, T.Z. Ming, W.Q. Shen, X.F. Yu, Heat transfer enhancement on a microchannel heat sink with impinging jets and dimples, Int. J. Heat Mass Transf. 112 (2017) 113–124.

[37] T.Z. Ming, C.J. Cai, W. Yang, W.Q. Shen, W. Feng, N. Zhou, Optimization of dimples in microchannel heat sink with impinging jets-part B: the influences of dimple height and arrangement, J. Therm. Sci. 27 (2018) 321–330.

[38] T.Z. Ming, C.J. Cai, W. Yang, W.Q. Shen, T. Gan, Optimization of dimples in microchannel heat sink with impinging jets – Part A: Mathematical model and the influence of dimple radius, J. Therm. Sci. 27 (2018) 195–202.

[39] T.W. Wei, H. Oprins, V. Cherman, E. Beyne, M. Baelmans, Experimental and numerical investigation of direct liquid jet impinging cooling using 3D printed manifolds on lidded and lidless packages for 2.5D integrated systems, Appl. Therm. Eng. 164 (2020).

[40] K.P. Drummond, D. Back, M.D. Sinanis, D.B. Janes, D. Peroulis, J.A. Weibel, S. V. Garimella, A hierarchical manifold microchannel heat sink array for high-heat-flux two-phase cooling of electronics, Int. J. Heat Mass Transf. 117 (2018) 319–330.

[41] C.S. Sharma, G. Schlottig, T. Brunschwiler, M.K. Tiwari, B. Michel, D. Poulikakos, A novel method of energy efficient hotspot-targeted embedded liquid cooling for electronics: an experimental study, Int. J. Heat Mass Transf. 88 (2015) 684–694.

[42] C.S. Sharma, M.K. Tiwari, S. Zimmermann, T. Brunschwiler, G. Schlottig, B. Michel, D. Poulikakos, Energy efficient hotspot-targeted embedded liquid cooling of electronics, Appl. Energy 138 (2015) 414–422.

[43] D. Ansari, K.Y. Kim, Hotspot thermal management using a microchannel-pinfin hybrid heat sink, Int. J. Therm. Sci. 134 (2018) 27–39.

[44] Y.J. Lee, P.S. Lee, S.K. Chou, Hotspot mitigating with obliquely finned microchannel heat sink-an experimental study, IEEE Trans. Compon. Packag. Manuf. Technol. 3 (2013) 1332–1341.

[45] T. Brunschwiler, H. Rothuizen, S. Paredes, B. Michel, P. Bezama, Hotspot-adapted cold plates to maximize system efficiency. International Workshop on Thermal Investigations of Ics & Systems, 2009.

[46] H.C. Cui, X.T. Lai, J.F. Wu, M.Z. Wang, W. Liu, Z.C. Liu, Overall numerical simulation and experimental study of a hybrid oblique-rib and submerged jet impingement/microchannel heat sink, Int. J. Heat Mass Transf. 167 (2021) 120839.

[47] M.A.R. Sharif, A. Banerjee, Numerical analysis of heat transfer due to confined slot-jet impingement on a moving plate, Appl. Therm. Eng. 29 (2009) 532–540.
[48] J.H. Shin, T. Rozenfeld, T. Shockner, A.K. Vutha, Y.Y. Wang, G. Ziskind, Y. Peles, Local heat transfer under an array of micro jet impingement using HFE-7000, Appl. Therm. Eng. 158 (2019) 113716.
[49] P. Xu, A.P. Sasmito, S.X. Qiu, A.S. Mujumdar, L. Xu, L.P. Geng, Heat transfer and entropy generation in air jet impingement on a model rough surface, Int. Commun. Heat Mass Transf. 72 (2016) 48–56.
[50] Z.R. Chi, H.Q. Liu, S.S. Zang, Geometrical optimization of nonuniform impingement cooling structure with variable-diameter jet holes, Int. J. Heat Mass Transf. 108 (2017) 549–560.
[51] R. Wu, Y. Fan, T. Hong, H. Zou, R. Hu, X. Luo, An immersed jet array impingement cooling device with distributed returns for direct body liquid cooling of high power electronics, Appl. Therm. Eng. 162 (2019) 114259.
[52] S.V. Alekseenko, A.V. Bilsky, V.M. Dulin, D.M. Markovich, Experimental study of an impinging jet with different swirl rates, Int. J. Heat Fluid Flow 28 (2007) 1340–1359.
[53] T.A. Trabold, N.T. Obot, Impingement heat transfer within arrays of circular jets: Part II—Effects of crossflow in the presence of roughness elements, J. Turbomach. 109 (1987) 594.
[54] G.D. Xia, J. Jiang, J. Wang, Y.L. Zhai, D.D. Ma, Effects of different geometric structures on fluid flow and heat transfer performance in microchannel heat sinks, Int. J. Heat Mass Transf. 80 (2015) 439–447.